

# Microphysical Constraints on Millimeter-Wavelength Scattering Properties of Snow Particles

NORMAN B. WOOD

*Cooperative Institute for Meteorological Satellite Studies, University of Wisconsin–Madison, Madison, Wisconsin*

TRISTAN S. L'ECUYER

*Department of Atmospheric and Oceanic Sciences, University of Wisconsin–Madison, Madison, Wisconsin*

ANDREW J. HEYMSFIELD

*National Center for Atmospheric Research,\* Boulder, Colorado*

GRAEME L. STEPHENS

*NASA Jet Propulsion Laboratory, California Institute of Technology, Pasadena, California*

(Manuscript received 13 May 2014, in final form 22 November 2014)

## ABSTRACT

A Bayesian optimal estimation retrieval is used to determine probability density functions of snow microphysical parameters from ground-based observations taken during four snowfall events in southern Ontario, Canada. The retrieved variables include the parameters of power laws describing particle mass and horizontally projected area. The results reveal nontrivial correlations between mass and area parameters that were not apparent in prior studies. The observations provide information mainly about the mass coefficient  $\alpha$ , somewhat less information about the mass exponent  $\beta$  and the projected area coefficient  $\gamma$ , and minimal information about the projected area exponent  $\sigma$ . The expected values for retrieved mass power-law parameters  $\alpha = 0.00328$  and  $\beta = 2.25$  are consistent with those from several prior studies that looked at the mass of aggregate-like particles and precipitating ice aloft as functions of maximum particle dimension. Differences from other studies appear related to differences in the dimensions used to define particle size. The retrieval allows the analysis of relatively large volumes of continuous observations, greatly enhancing sampling relative to single-particle analyses. The retrieved properties are used to constrain 94-GHz (W band) radar scattering properties for a variety of snow particle shapes. Synthetic reflectivities calculated using these scattering properties and observed particle size distributions show that a branched, spatial aggregate-like particle produces good agreement with coincident observed W-band reflectivities. Uncertainties in the synthetic reflectivities, estimated by applying a simple error-propagation model, are substantial and are dominated by the uncertainties in  $\alpha$  and  $\beta$ .

## 1. Introduction

Millimeter-wavelength (e.g., Ka and W band) radars have use for the remote sensing of precipitation, especially from space-based platforms owing to their

sensitivity and relatively compact form (Mead et al. 1994). *CloudSat* (Stephens et al. 2008), for example, operates a nadir-viewing W-band profiling radar that observes latitudes from 82°N to 82°S, making it an important platform for sensing high-latitude precipitation. Scattering by precipitation-sized ice particles at these wavelengths, however, is sensitive to particle shape as well as mass, and accounting for the variation of snow microphysical properties and shapes is a substantial difficulty for retrieving snowfall with these instruments. Such retrieval problems require a priori assumptions about the microphysical and scattering properties of observed snowfall. To adequately characterize uncertainties in snowfall retrievals,

---

\*The National Center for Atmospheric Research is sponsored by the National Science Foundation.

---

Corresponding author address: Norman B. Wood, Cooperative Institute for Meteorological Satellite Studies, University of Wisconsin–Madison, 1225 West Dayton Street, Madison, WI 53706.  
E-mail: norman.wood@ssec.wisc.edu

the a priori information must characterize the variability of these properties as well as their expected values.

For snowfall at the surface, microphysical properties have typically been evaluated using time-consuming analyses of individual particles (e.g., [Mitchell et al. 1990](#); [Heymssfield and Westbrook 2010](#)). The limited sampling in such an approach makes it difficult to characterize the expected values and variability of these properties. As an alternative, several recent field campaigns, including ground validation studies associated with satellite missions ([Hudak et al. 2006](#); [L'Ecuyer et al. 2010](#); [Hudak et al. 2012](#)) as well as a stand-alone study ([Löhnert et al. 2011](#)), have made intensive observations of snowfall properties using nearly collocated radars, disdrometers, and precipitation gauges. Although the locations sampled by these campaigns are currently limited, such observations offer the potential to characterize snowfall properties in varied locations and meteorological regimes.

[Wood et al. \(2014, hereinafter W14\)](#) introduced an optimal estimation (OE; [Rodgers 2000](#)) retrieval for analyzing such observations. The retrieval produces Gaussian probability density functions (PDFs) representing the expected values and uncertainties for parameters describing the variation of particle mass  $m$  and horizontally projected area  $A_p$  with particle size. Such PDFs have value as explicit a priori constraints for remote sensing retrievals, and may also be used to characterize uncertainties in scattering properties caused by uncertainties in microphysical properties. Determining mass and  $A_p$  parameters simultaneously ensures their physical consistency, and the automation of most of the relevant measurements ensures substantial sampling during snowfall events.

This work characterizes snow microphysical properties via the [W14](#) retrieval, and then applies those properties to investigate the modeling of radar scattering properties of snow particles. Observations of snowfall rate, snow particle size distribution, size-resolved fall speeds, and 9.35-GHz (X band) radar reflectivity are used to estimate the parameters of power laws describing particle mass and  $A_p$  as functions of particle size. The retrieval is applied to four midlatitude snowfall events from the Canadian *CloudSat/CALIPSO* Validation Project (C3VP; [Hudak et al. 2006](#)). The retrieved PDFs of snow microphysical parameters are then applied to constrain particle models used to evaluate W-band radar scattering properties via the discrete dipole approximation ([Draine and Flatau 1994](#)), and the performance of these models is evaluated using ground validation observations.

## 2. C3VP events

The snow events used in this work were observed at the Meteorological Service of Canada's Centre for

Atmospheric Research Experiments (CARE) at Egbert, Ontario, Canada, approximately 80 km north of Toronto. Observations used as inputs to the retrieval consist of 9.35-GHz radar reflectivities from the McGill University vertically pointing X-band radar (VertiX; [Fabry and Zawadzki 1995](#)), snowfall rates from a Vaisala, Inc., FD12P ([Vaisala Oyj 2002](#)) scaled to match snow accumulations from a double fence intercomparison reference (DFIR; [Goodison et al. 1998](#)), size-resolved fall speeds from Colorado State University's 2D video disdrometer (2DVD; [Kruger and Krajewski 2002](#); [Huang et al. 2010](#)), and size distributions from the National Aeronautics and Space Administration's Snowflake Video Imager (SVI; [Newman et al. 2009](#)). The characteristics of these observations are described more completely in [W14](#).

Four snowfall events were selected because of completeness of the required observations and because they represent a modest range of snowfall conditions. Observations by personnel on the ground at CARE ([R. T. Austin et al. 2007](#), unpublished manuscript) along with daily operations logs ([CIRA 2013](#)) from the 10th Cloud Layer Experiment (CLEX-10), which operated jointly with C3VP, provide characteristics of three of the events. Synoptic event 1 (SYN1; 6 December 2006) involved a weak low passing northeastward over Ontario that produced snowfall at CARE mainly between about 1200 and 1530 UTC. Aircraft observations near CARE showed liquid phase near cloud top with mixed phase and ice below. Snowfall at CARE was described as light and dry early in the day transitioning to moderate wet snow later. VertiX echo-top heights were about 4 km above ground level (AGL) during the precipitation and SVI size distributions showed tails extending to 4–8 mm ([Fig. 1](#)). Temperatures during the most significant snowfall were near freezing. The 24-h accumulation for the event was 3.2 mm liquid water equivalent (LWE).

Lake-effect event 1 (LE1; 7 December 2006) consisted of lake-effect snow squalls that resulted from the cold air mass and northwesterly winds that followed the system of the previous day. CARE received snowfall over most of the day, with a 24-h accumulation of 10.2 mm LWE. Temperatures were near freezing early in the day and decreased with time, reaching 255 K at the day's end ([Fig. 2](#)). VertiX echo-top heights were shallower than the previous day, varying from 1 to 3 km AGL. SVI size distributions were similar to those of the previous day but more variable over time. A period after 2100 UTC showed high concentrations of particles smaller than 2 mm and was associated with the coldest temperatures of the day.

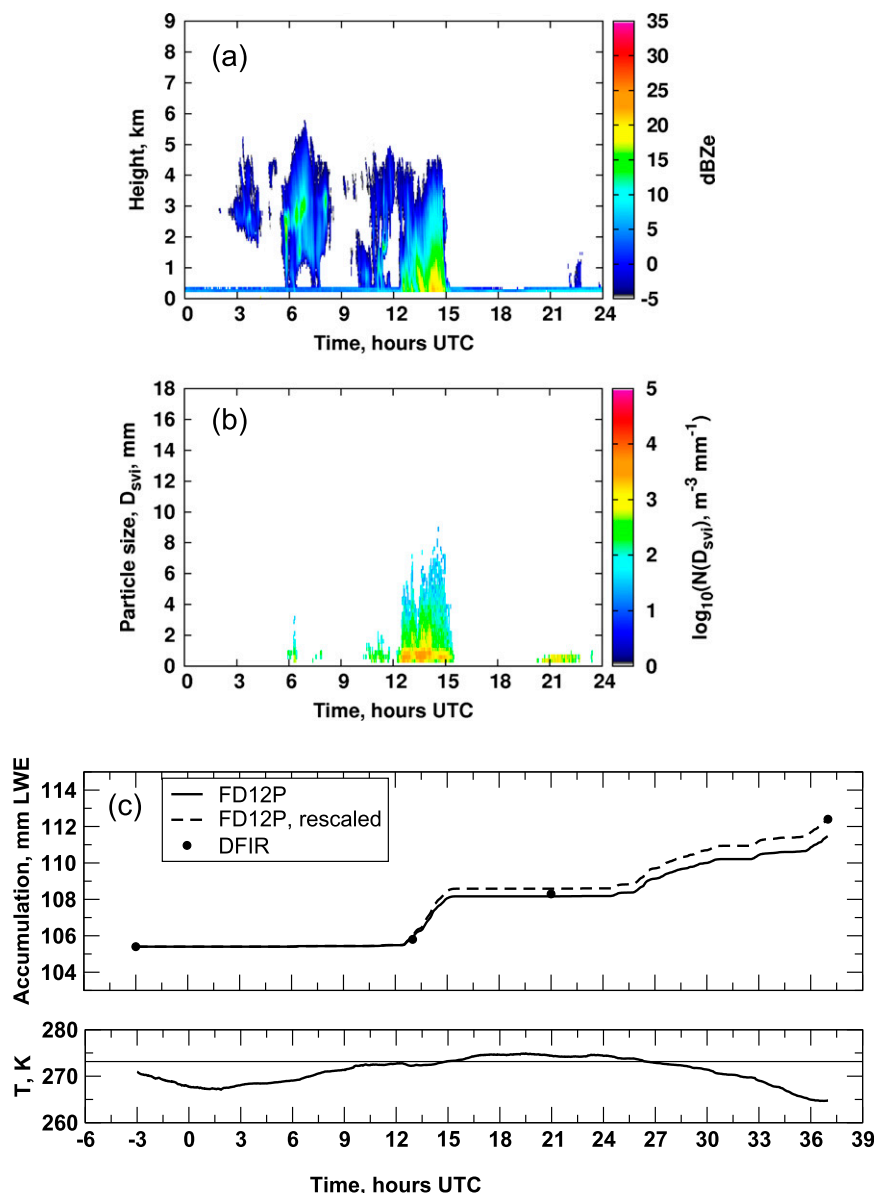


FIG. 1. C3VP observations for event SYN1. (a) VertiX reflectivity, (b) SVI size distributions, and (c) snow accumulations and 2-m air temperature.

Lake-effect event 2 (LE2; 27–28 January 2007) was a second lake-effect snow event that resulted as a warm front near CARE shifted to the south during the evening of 27 January and cold northwesterly winds entered the area. Snow fell mainly between 0100 and 0400 UTC, at temperatures between 267 and 270 K. Snowfall rates at CARE were initially light, but increased rapidly as a heavy snowband lingered over the site (Fig. 3). Large snowflakes, near 10 mm in diameter, fell during periods of heavy snow and visibility was near zero. SVI size distributions showed particles with sizes up to 10 mm early in the event. Total accumulations for the day were 4.6 mm LWE.

Synoptic event 2 (SYN2; 14 February 2007) occurred between intensive observing periods. Although C3VP observer reports of the conditions on the surface and aloft are lacking, the event has been recognized as a massive synoptic winter storm, producing extensive snowfall with substantial accumulations and societal impacts over northeastern United States and southeastern Canada (Grumm and Stuart 2007). At CARE, this system was significantly deeper than the other three events, with VertiX echo-top heights extending to about 6 km AGL (Fig. 4). Observations from precipitation gauges show that snowfall occurred throughout most of

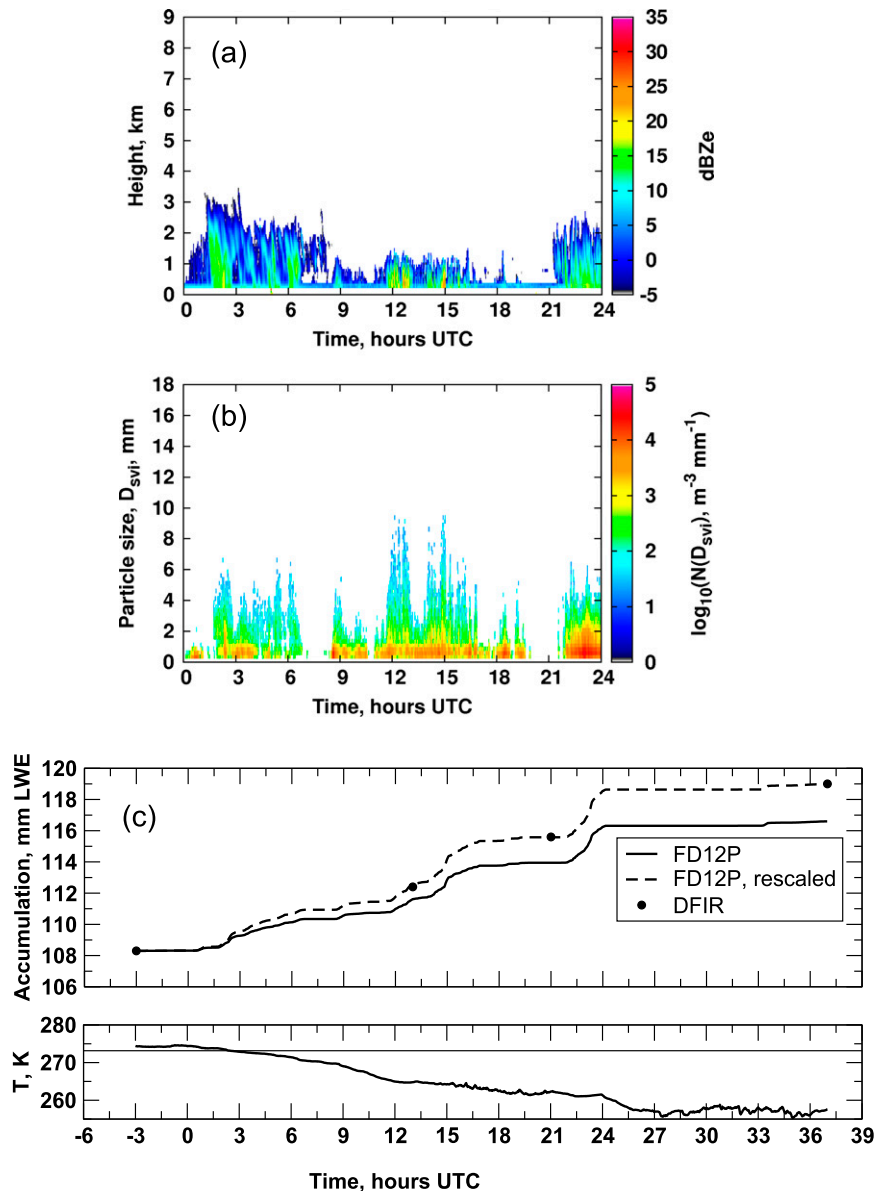


FIG. 2. As in Fig. 1, but for event LE1.

the day and produced accumulations of 8.3 mm LWE. This event was also the coldest of the four, with temperatures ranging from 256 to 261 K during the snowfall and with SVI size distributions that were narrow in comparison with those of the earlier events. Characteristics of the events are summarized in Table 1.

The causes for the large DFIR/FD12P accumulation ratios for events LE2 and SYN2 (Table 1) are not clear. The FD12P uses both an optical sensor and a heated capacitive sensor to estimate precipitation rates for snow and the capacitive sensor is subject to undercatch (Vaisala Oyj 2002). For event LE2, however, winds observed at the CARE meteorological tower were light

at  $0.5\text{--}2.5\text{ m s}^{-1}$  during the snowfall, suggesting that undercatch should not have been significant. Winds were stronger for event SYN2, generally below  $5\text{ m s}^{-1}$ , but ranging as high as  $6\text{ m s}^{-1}$  for short periods. Additionally, the size distributions for event SYN2 suggest high concentrations of small particles were present (Fig. 4). For this event, undercatch by the capacitive sensor may have been significant and biased the unscaled FD12P precipitation rates low.

Observations were averaged over independent 5-min samples and uncertainties estimated as described in Wood et al. (2013) and W14. Ground clutter caused the nearest usable VertiX reflectivities to be 488 m above

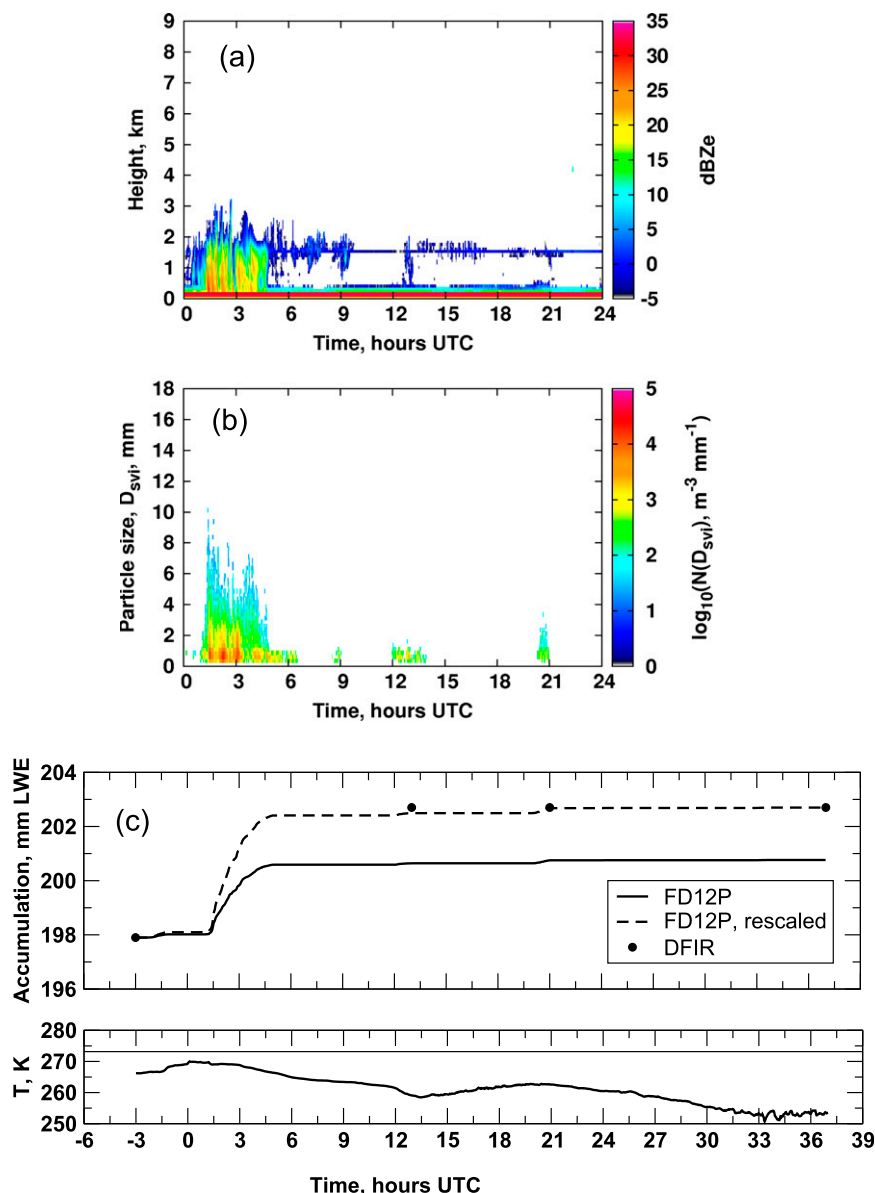


FIG. 3. As in Fig. 1, but for event LE2.

the ground. From the reflectivities at 488 m, reflectivities at the surface and the corresponding uncertainties were estimated by considering vertical reflectivity gradients and the likely time separation between precipitation features observed aloft and their appearance at the surface, as described by W14. The resulting samples were then screened to ensure temperatures less than 273 K and wind speeds less than  $5 \text{ m s}^{-1}$  at the surface, giving 375 distinct samples from the four events: 33 from event SYN1, 173 from LE1, 43 from LE2, and 126 from SYN2.

The VertiX observations are susceptible to attenuation by wet snow accumulations on the radar's conically

shaped radome. Wet snowfall may have occurred for event SYN1 from roughly 1200 to 1500 UTC, and for event LE1 from 0000 to 0400 UTC, during periods of near-freezing temperatures. The VertiX was monitored and cleared of snow periodically, but the times at which this was done are not known. Comparisons of time series of observations over the CARE site by Environment Canada's King City radar against coincident VertiX observations suggest the VertiX experienced about 2 dB of attenuation by the end of the SYN1 period. For the LE1 event, the time series comparisons suggest about 4 dB of attenuation, but it appears the radome was cleared after 0400 UTC, prior to the remaining 20 h of

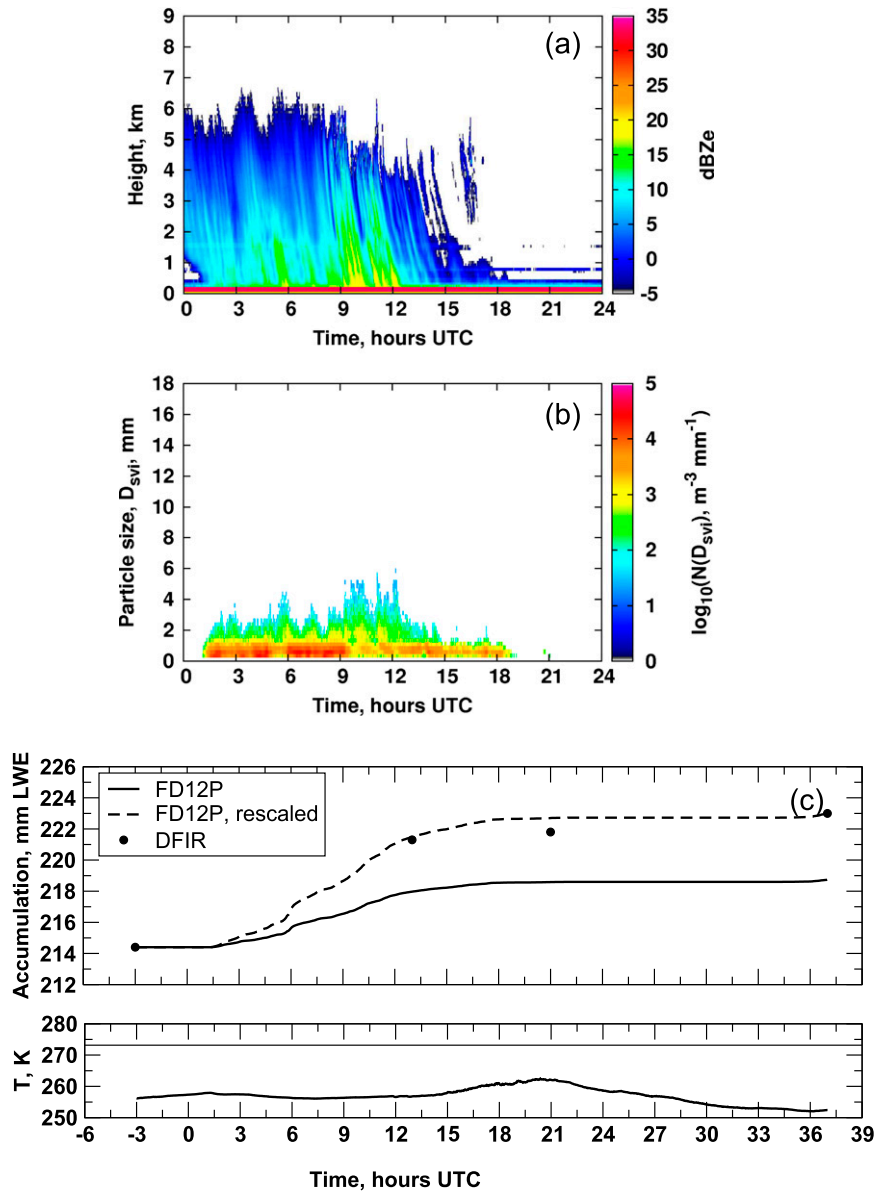


FIG. 4. As in Fig. 1, but for event SYN2.

LE1 observations. Bias corrections for the VertiX observations were determined using these King City radar comparisons, as described in W14, and provide partial compensation for this attenuation.

### 3. The snow microphysics retrieval

The retrieval, described and evaluated by W14 using synthetic observations, assumes that particle mass  $m$  and horizontally projected area  $A_p$  can be related to particle size using power laws (e.g., Mitchell 1996):

$$m(D_M) = \alpha D_M^\beta \quad \text{and} \quad (1)$$

$$A_p(D_M) = \gamma D_M^\sigma, \quad (2)$$

where  $D_M$  is the particle maximum dimension, the distance between the two farthest-separated points on the particle's surface, and  $A_p$  is simply the area of the projection of the particle's shape onto the plane normal to the particle's downward motion. For a given sample of the observations, the retrieval gives the joint distribution of  $\alpha$ ,  $\beta$ ,  $\gamma$ , and  $\sigma$ , as well as one additional variable  $\phi$ . This additional variable relates the particle dimension  $D_{\text{obs}}$  observed by a particular disdrometer to  $D_M$ , compensating for the varying ability of disdrometers to measure the true

TABLE 1. Properties of C3VP events. Fraction of day snowing is the fraction of time for which the surface observations of precipitation rate are nonzero. Time is approximate time over which retrievals were performed. The max rate and day accumulation were evaluated using 1-min FD12P rates rescaled to match DFIR accumulations. Max  $Z_e$  was taken from the 10-s VertiX data for range bin 13 at 488 m AGL.

	Event			
	SYN1	LE1	LE2	SYN2
Date	6 Dec 2006	7 Dec 2006	28 Jan 2007	14 Feb 2007
Fraction of day snowing	0.25	0.80	0.27	0.81
Time (UTC)	1230–1530	0000–2359	0100–0500*	0130–1730
Max rate (mm LWE h <sup>-1</sup> )	2.7	5.2	5.9	3.3
Day accumulation (mm LWE)	3.2	10.2	4.6	8.3
DFIR/FD12P accumulation ratio	1.15	1.29	1.68	1.98
Max $Z_e$ (dB)	21.3	25.5	28.8	19.7
VertiX echo-top height (km)	4.0	1.75–3.0 (1.0–1.5)**	2.5	6.0–3.0

\* Retrievals also include several results from near 2037 UTC.

\*\* For intermittent lake-effect snowbands.

dimensions of particles of different shapes (Wood et al. 2013):

$$D_M \approx D_{\text{obs}}/\phi, \quad (3)$$

with the measured size distributions transformed as

$$N(D_M) \approx \phi N(D_{\text{obs}}). \quad (4)$$

A single value of  $\phi$  is applied over all particle sizes in any observed distribution. Together, these variables form the state vector  $\mathbf{x}$ , whose PDF is to be retrieved,

$$\mathbf{x} = [\ln(\alpha) \quad \beta \quad \ln(\gamma) \quad \sigma \quad \phi]^T, \quad (5)$$

where  $\alpha$  and  $\gamma$  have been log transformed because of their large range and the need for their distributions to approximate the Gaussian shape.

To find the retrieved estimate  $\hat{\mathbf{x}}$  of the state, the cost function

$$\begin{aligned} \Phi(\mathbf{x}, \mathbf{y}, \mathbf{x}_a) = & [\mathbf{y} - \mathbf{F}(\mathbf{x}, \tilde{\mathbf{b}})]^T \mathbf{S}_e^{-1} [\mathbf{y} - \mathbf{F}(\mathbf{x}, \tilde{\mathbf{b}})] \\ & + (\mathbf{x} - \mathbf{x}_a)^T \mathbf{S}_a^{-1} (\mathbf{x} - \mathbf{x}_a) \end{aligned} \quad (6)$$

is minimized with respect to  $\mathbf{x}$  using Newtonian iteration (Rodgers 2000). The observation vector  $\mathbf{y}$  contains 9.35-GHz radar reflectivity, snowfall rate, and three measures derived from fall speeds observed in size bins centered at  $D_M$  values of 4, 2, and 1 mm (W14). The forward model  $\mathbf{F}(\mathbf{x}, \tilde{\mathbf{b}})$  approximates the true physical relation between  $\mathbf{x}$  and  $\mathbf{y}$ , and may require other influence parameters  $\tilde{\mathbf{b}}$ , where the tilde indicates these parameters may be known imperfectly. In particular, this forward model, described more completely in W14, takes trial values of the elements

of the state vector  $\mathbf{x}$ , then uses the observed particle size distribution (PSD) to simulate X-band reflectivity, snowfall rate, and the three fall speed measures for comparison against the observed values in  $\mathbf{y}$ . The covariance matrix  $\mathbf{S}_e$  represents the combined measurement and forward model uncertainties as a multivariate Gaussian distribution. Prior information about the state vector is represented with the vector of expected values  $\mathbf{x}_a$  and their covariances  $\mathbf{S}_a$  (Table 2), also as a multivariate Gaussian distribution. W14 provides an assessment of the a priori state and uncertainties for the retrieval. At convergence, a  $\chi^2$  statistic is calculated by applying  $\hat{\mathbf{x}}$  in (6), and a value near  $N_y$ , the number of observations, suggests correct convergence.

Selecting Gaussian distributions acknowledges the limited information available about the actual forms of these distributions, and also leads to a reasonably tractable form for the retrieval. For distributions with specified widths, Gaussian distributions maximize the entropy of the distribution (Rodgers 2000; Shannon and Weaver 1949) and impose the least constraint on the retrieval. Selecting other PSD forms without evidence of their appropriateness would introduce unjustified constraints.

The retrieval also estimates the error covariance matrix for the retrieved state vector  $\hat{\mathbf{x}}$ ,

TABLE 2. Estimates of the a priori state for mass- and area-dimension parameters for use in the C3VP microphysics retrieval.

Parameter	Means	Correlation	Variances	Covariances
$\ln(\alpha)$	-6.18	0.75	2.47	0.59
$\beta$	2.07		0.24	
$\ln(\gamma)$	-1.56	0.84	0.39	0.12
$\sigma$	1.79		0.05	



$$\hat{\mathbf{S}}_x = \begin{Bmatrix} s^2[\ln(\alpha)] & s[\ln(\alpha), \beta] & s[\ln(\alpha), \ln(\gamma)] & s[\ln(\alpha), \sigma] & s[\ln(\alpha), \phi] \\ & s^2[\beta] & s[\beta, \ln(\gamma)] & s[\beta, \sigma] & s[\beta, \phi] \\ & & s^2[\ln(\gamma)] & s[\ln(\gamma), \sigma] & s[\ln(\gamma), \phi] \\ & & & s^2[\sigma] & s[\sigma, \phi] \\ & & & & s^2[\phi] \end{Bmatrix}, \quad (7)$$

where only the upper triangular portion is shown,  $s^2[\cdot]$  are variances in retrieved parameters, and  $s[\cdot]$  are the covariances between them.

Together,  $\hat{\mathbf{x}}$  and  $\hat{\mathbf{S}}_x$  describe a five-dimensional Gaussian PDF that represents the retrieved state. Values for  $\alpha$ ,  $\beta$ ,  $\gamma$ , and  $\sigma$  in this work are in cgs units, with  $D_M$  in centimeters and  $\alpha$  and  $\gamma$  taking appropriate units to give mass in grams and  $A_p$  in square centimeters. The results for each event were composited by Monte Carlo sampling from each retrieved PDF within the event, then evaluating the mean values and covariance matrix for the pooled sample. Ten realizations were performed and the resulting means and covariance matrices averaged to obtain final values. Retrievals were performed in two different configurations, representing two different fall speed forward models [MH05, from Mitchell and Heymsfield (2005), and HW10, from Heymsfield and Westbrook (2010), as described in W14]. The results presented here are for the MH05 configuration except as noted, but results for the HW10 configuration were similar.

#### 4. Snow microphysics retrieval results

Considering the mass parameters, retrieved values of  $\beta$  range mainly from 1.75 to 2.75 and  $\alpha$  from about 0.001 to 0.01, with  $\ln(\alpha)$  and  $\beta$  positively correlated (Fig. 5). The pooled means and standard deviations, taken as the square roots of diagonal elements of the pooled covariance matrices, are indicated by the blue error bars. The black triangles in Fig. 5a show parameter values compiled by Mitchell (1996) for a range of particle shapes (Table 3). The retrieved values from this study are similar to those from Mitchell for several shapes associated with large, irregularly shaped particles: densely rimed dendrites (R2b), aggregates (S3 and S1a), rosettes (C2a), and side planes (S1), where the terms in parentheses are the corresponding habit designations from Magono and Lee (1966). For all events, the pooled standard deviations are substantially smaller than the a priori standard deviations (gray bars), suggesting the mass parameters are well constrained by the observations, particularly  $\ln(\alpha)$ .

Differences between events are apparent in the mass parameters, with values for the two synoptic events (SYN1 and SYN2) larger than those for the lake-effect

events (LE1 and LE2). The strongest contrasts are between events SYN1 and LE2. The mass parameter pooled means for these two events differ by almost a full standard deviation in both  $\beta$  and  $\ln(\alpha)$ , perhaps capturing differences in the meteorological conditions producing the snowfall. In spite of the differences, the reflectivity values for the two events are similar, as indicated by the sizes of the plotted points in Fig. 5. In contrast, while event SYN2 was also a synoptic-scale event and has parameters similar to event SYN1, it is characterized by much smaller reflectivities and temperatures than is event SYN1. The narrow PSDs observed for event SYN2 (Fig. 4) suggest weak aggregation, in contrast to the broader observed PSDs and the large, sticky particles reported by ground personnel at CARE for event SYN1; however, an examination of the SVI images shows substantial numbers of irregular, aggregate-like particles with  $D = 1$  to 5 mm for event SYN2. In contrast to the other events, event LE1 has a more mixed range of temperatures and reflectivities, and has retrieved parameters falling between those of the two synoptic events SYN1 and SYN2 and the other lake-effect snow event LE2.

Unlike the mass parameters, the area parameters  $\gamma$  and  $\sigma$  are similar among the events and differ only slightly from the a priori estimates (Fig. 6). The pooled standard deviations are also similar to the a priori values. Overall, these results suggest the observations provide some information about the area parameters but constrain them only weakly. Again, values from Mitchell (1996) that represent larger, irregular particles are shown for comparison (Fig. 6a, black triangles). The two points nearest the expected values for the retrieved state correspond to densely rimed dendrites (R2b), aggregates (S3 and S1a), rosettes (C2a), and side planes (S1) (Table 3), the same shapes that best matched the results for the mass parameters.

For  $\phi$ , smaller values are associated with narrower distributions (Fig. 7), where  $\lambda$  values in this plot were obtained using weighted orthogonal distance regression (Boggs et al. 1992) to fit the observed SVI size distributions to the log transformed form of the negative exponential size distribution, with weights based on uncertainties calculated following Wood et al. (2013). There is also a trend toward smaller values of  $\phi$  with decreasing temperatures, with the smallest values of  $\phi$  associated with the coldest event, SYN2. The pooled



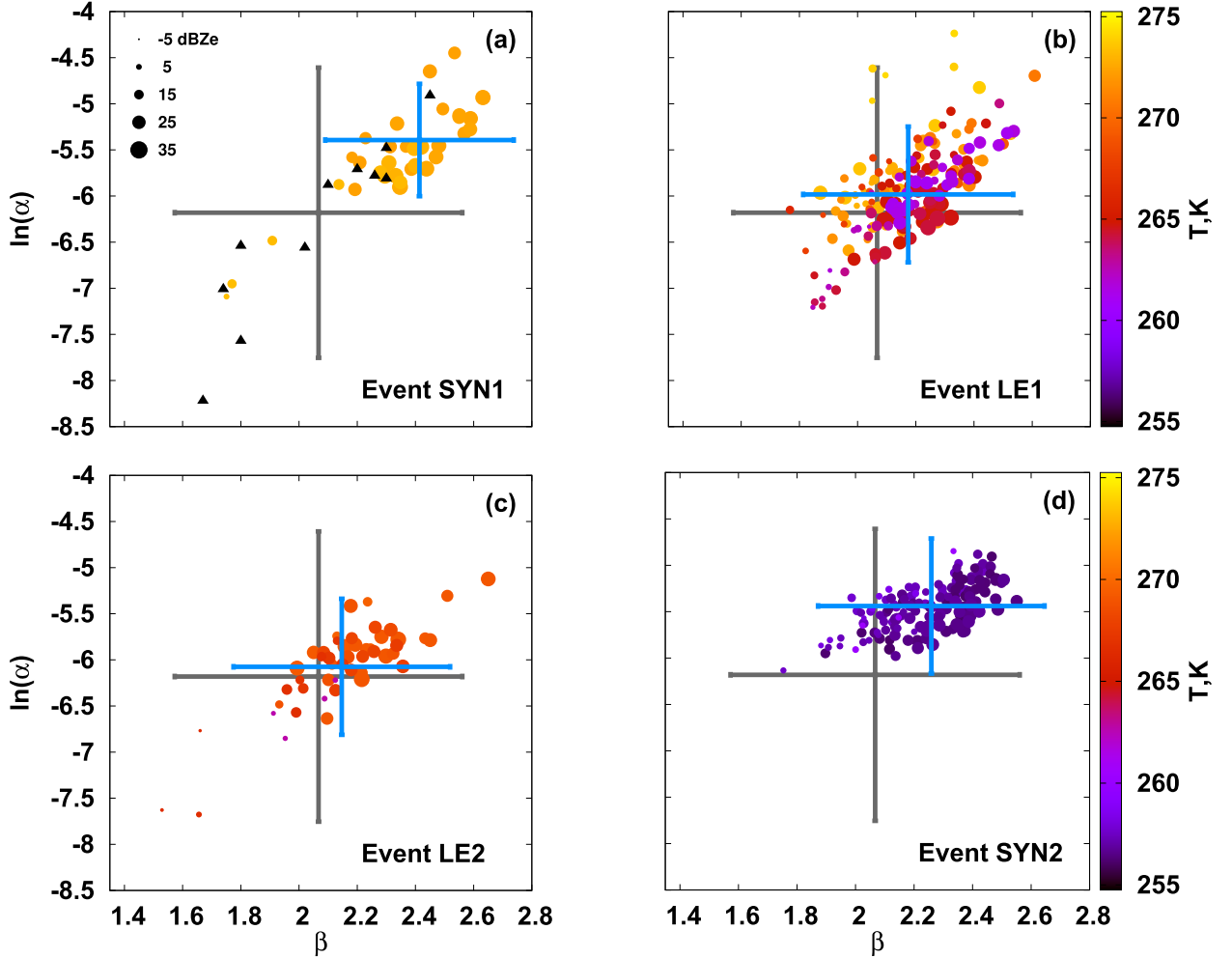


FIG. 5. Retrieved mass parameters for events (a) SYN1, (b) LE1, (c) LE2, and (d) SYN2. Points are sized and color coded to indicate the retrieval input values for reflectivity and temperature, respectively. Gray error bars show the a priori expected values and standard deviations; blue bars show them for the retrieved state. Black triangles in (a) show values from Mitchell (1996) for larger and irregularly shaped particles.

standard deviations are somewhat smaller than the a priori value, suggesting the observations weakly constrain this parameter. The pooled mean values are smaller than the a priori and vary somewhat among the events. For the SVI, reductions in  $\phi$  are associated with reductions in particle aspect ratios (Wood et al. 2013). The trend toward smaller  $\phi$  with narrower distributions and colder temperatures would be consistent with a trend from aggregate to more pristine particles, but the differences among the a priori and event-specific values are small compared to the standard deviations.

A pooled estimate was also produced for all four events combined, following the process described above. Because the number of retrievals per event varied considerably, weights were applied to the sampled points to balance the importance of the events, giving as results

$$\hat{\mathbf{x}} = [-5.72 \quad 2.25 \quad -1.38 \quad 1.81 \quad 0.78]^T, \quad (8)$$

with the covariance matrix

$$\hat{\mathbf{S}}_x = \begin{bmatrix} 0.59 & 0.21 & 0.09 & 0.02 & 0.03 \\ 0.21 & 0.14 & 0.01 & 0.01 & 0.01 \\ 0.09 & 0.01 & 0.34 & 0.10 & 0.01 \\ 0.02 & 0.01 & 0.10 & 0.05 & 0.00 \\ 0.03 & 0.01 & 0.01 & 0.00 & 0.01 \end{bmatrix}. \quad (9)$$

As anticipated from Figs. 5–7, the variances and covariances associated with the mass parameters have decreased compared to the a priori, while those associated with the area parameters and  $\phi$  have changed little (Table 4). The posterior state for the HW10 configuration is essentially unchanged from that for the MH05

TABLE 3. Mass and area parameters from Mitchell (1996) used in Figs. 5 and 6. Corresponding habit codes are from Magono and Lee (1966). S1a indicates aggregates of side planes. Particle dimensions are in micrometers, and the parameters are in cgs units.

Habit	$D_{\min}$	$D_{\max}$	$\beta$	$\ln(\alpha)$	$\sigma$	$\ln(\gamma)$
P1d	90	1500	1.67	-8.22	1.63	-2.21
N1e	300	—	1.74	-7.01	1.414	-2.97
P1c	100	1000	1.8	-7.57	1.76	-1.56
R1b	200	2400	1.8	-6.54	1.414	-2.97
P1b	40	2000	2.02	-6.56	1.97	-0.60
S3	800	4500	2.1	-5.88	1.88	-1.48
S1a	600	4100	2.2	-5.71	1.88	-1.48
C2a	200	1000	2.26	-5.78	1.57	-2.44
R2b	1800	4000	2.3	-5.81	1.76	-1.56
S1	300	2500	2.3	-5.48	1.88	-1.48
P1a	100	3000	2.45	-4.91	2.00	-0.43

configuration. Values for the diagonal elements of the averaging kernel matrix  $\mathbf{A}$ , a performance metric described in W14 for this retrieval, show that  $\ln(\alpha)$  is strongly constrained by the observations ( $\mathbf{A}$  values from 0.9 to 1.1),  $\beta$  and  $\ln(\gamma)$  are influenced by both the observations and the a priori ( $\mathbf{A}$  values of about 0.3), and  $\sigma$  and  $\phi$  primarily reproduce the a priori ( $\mathbf{A}$  values near 0.1).

One of the key questions to be answered by this analysis is whether covariances exist that were not present in the a priori. From (9), it can be seen that covariances that mix mass and area parameters {e.g.,  $s[\ln(\alpha), \ln(\gamma)]$ } are nonzero, whereas they were zero in the a priori. The corresponding correlation matrix (Fig. 8) shows nontrivial correlations between  $\ln(\alpha)$  and  $\ln(\gamma)$  ( $=0.20$ ), between  $\beta$  and  $\sigma$  ( $=0.09$ ), and between  $\ln(\alpha)$  and  $\sigma$  ( $=0.14$ ). The first two, in particular, likely arise because of the dependence of fall speed on the ratio of mass to  $A_p$  (Mitchell and Heymsfield 2005).

While the expected values of  $\alpha$  and  $\beta$  from this study are similar to estimates from Mitchell, they are considerably different from the often-used values described by Brown and Francis (1995) ( $\beta = 1.9$ ,  $\alpha = 0.00294$  in cgs units), which were taken from the results of Locatelli and Hobbs (1974). Locatelli and Hobbs reported these values for unrimed aggregates of bullets, columns and side planes, and also for aggregates of densely rimed dendrites or radiating assemblages of dendrites. Heymsfield et al. (2010), using aircraft observations from six field campaigns, have suggested that values of  $\beta$  near 2.1 are more appropriate for cloud and precipitating ice. They found corresponding values of  $\alpha$  (cgs units) of 0.00359 for warm-topped nonconvective clouds, 0.00574 for cold-topped nonconvective clouds, and 0.00630 for convectively generated clouds. The warm-topped cloud cases included observations from C3VP. The mass–dimension relations from Mitchell (1996) and Heymsfield et al. (2010) are all based on measurements of maximum

particle dimension, while Locatelli and Hobbs (1974) used the diameter of an equal-area circle.

Several other studies have suggested values of  $\alpha$  that are substantially larger than the value of 0.00311 from this study. Brandes et al. (2007) found  $\alpha = 0.00890$  and  $\beta = 2.1$  for snow along Colorado's Front Range; however, their particle size was an equivalent volume diameter obtained from 2DVD observations and likely substantially smaller than  $D_M$ . Further, their mass–dimension relation was given as a function of the size distribution median volume diameter, rather than actual particle size. Muramoto et al. (1995) presented a density relation that, based on their definition of particle volume, can be converted to a mass–dimension relation with  $\alpha = 0.00987$  and  $\beta = 2.594$ . For particle size, they used the width of the particle as observed by a side-viewing camera with no correction for viewing geometry, which also would underestimate  $D_M$  (Wood et al. 2013). Similar to Brandes et al. (2007), they presented their density relation as a function of the mean particle size of the observations, rather than as a function of actual particle size. Magono and Nakamura (1965) gave a density relation for observations of wet and dry snow. Using only their dry snow observations and converting their densities to masses using their definition of particle volume, a best-fit mass–dimension relation gives  $\alpha = 0.00907$  and  $\beta = 1.82$ . Constraining  $\beta$  to 2.25 gives  $\alpha = 0.00722$ . They collected the snow particles on a flat surface, measured the longest horizontal dimension and the dimension normal to that, and then used the geometric mean of those dimensions as the particle size. Again, this underestimates  $D_M$ .

These results suggest that differences in how particle size is measured can have a substantial impact on estimates of  $\alpha$ . Using  $\phi$  as defined in (3) and letting  $\alpha_M$  be the value of  $\alpha$  determined when particle size is given by  $D_M$ , the value  $\alpha'$  associated with some other measure of particle size  $D_{\text{obs}}$  can be evaluated using

$$\alpha' D_{\text{obs}}^\beta = \alpha_M D_M^\beta = \alpha_M \left( \frac{D_{\text{obs}}}{\phi} \right)^\beta = \left( \frac{\alpha_M}{\phi^\beta} \right) D_{\text{obs}}^\beta. \quad (10)$$

Estimating  $\phi$  as 0.8 and using the expected value of  $\beta$  of 2.25,  $\alpha'$  will be a factor of 1.7 larger than  $\alpha_M$ . A significant part of the differences in mass–dimension coefficients may therefore be explained by these differences in the treatment of particle size. Differences may also be due to the use of independent variables other than  $D_M$  (distribution median volume diameter or mean particle size).

## 5. Application to radar retrieval of snowfall

A primary goal of the preceding analysis is to provide observational constraints on mass and shape that can

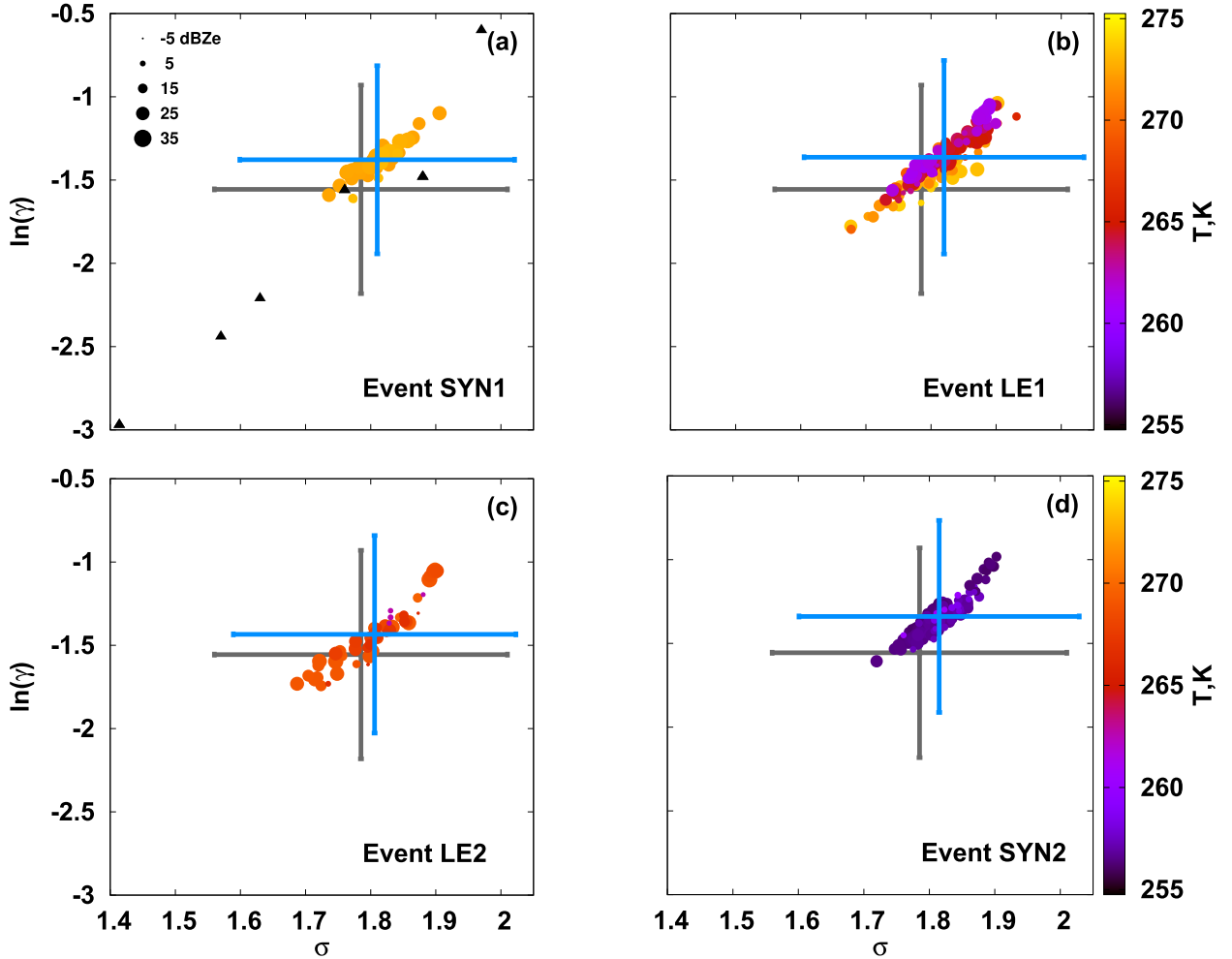


FIG. 6. As in Fig. 5, but for area parameters.

be used for modeling snow particle scattering properties and their uncertainties for use in millimeter-wavelength radar retrievals of snowfall rate. Using these observational constraints helps insure a physically consistent relationship between the particle microphysical and scattering properties that influence the relationships between radar reflectivity and snowfall rate that are assumed implicitly or explicitly within such retrievals.

Because of shape sensitivity, the Rayleigh or Mie approaches commonly used to model scattering properties at lower frequencies are not applicable for other than small particles (Schneider and Stephens 1995; Liu and Illingworth 1997). Scattering properties of larger snow particles may be simulated with Mie theory using spheres composed of a mixture of air and ice (the soft sphere approximation); however, comparisons against less approximate methods have shown the inability of such models to reproduce

backscattering properties across multiple frequencies (Petty and Huang 2010). Several more complex techniques may be used at millimeter wavelengths (see, e.g., Bohren and Singham 1991 for an overview). The discrete dipole approximation (DDA; Draine 1988; Draine and Flatau 1994), the method used for this work, allows for arbitrary geometry by replacing the continuous particle with an array of discrete dipoles on a spatial lattice.

The relationships for particle mass and  $A_p$  given by (8) do not fully constrain particle shape, so additional assumptions about shape are required before DDA calculations can be made. For millimeter wavelengths, it is likely that the scattering properties are not strongly sensitive to the fine structure of the spatial distribution of mass but will be sensitive to the larger-scale structure (Matrosov 2007). The objective of an assumed particle shape should be to reasonably capture the gross features of the spatial distribution of mass, rather than replicate

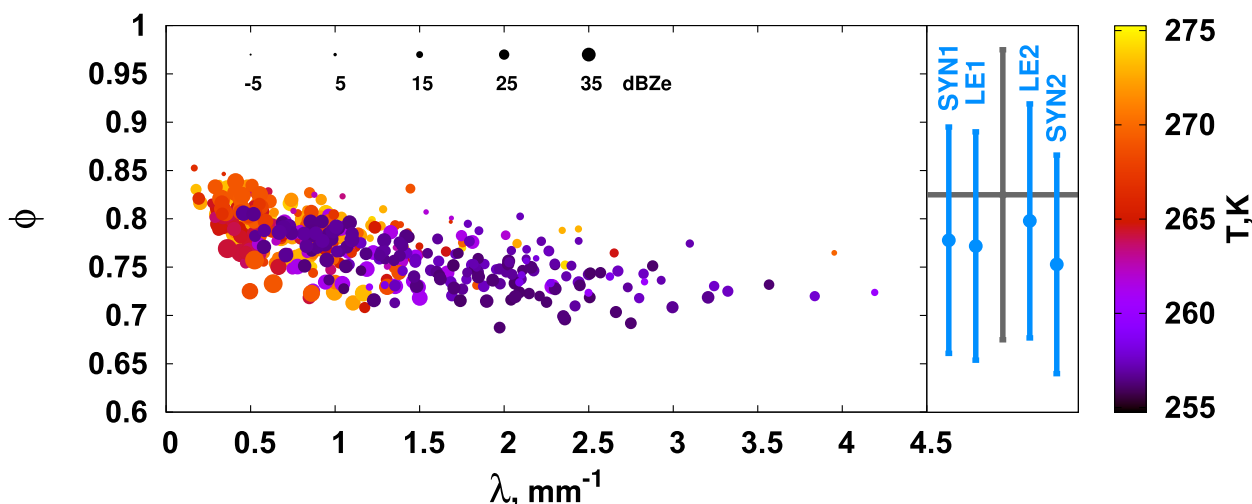


FIG. 7. (left) Retrieved shape parameters  $\phi$  vs size distribution slope  $\lambda$  fitted to the SVI-observed size distributions. Point sizes and colors for points and error bars are as in Fig. 5. (right) A priori (vertical gray bar) and event-pooled means and standard deviations (blue points and vertical bars).

particular fine features. The method for constraining DDA particle models using an assumed shape and the retrieved mass and  $A_p$  relationships is described in the appendix. Here we describe the various shape assumptions examined in this work, then present and assess the DDA results.

#### a. Shape assumptions

Using constrained DDA particle models (appendix), scattering calculations were made for a variety of shapes intended to represent the features of more pristine, planar particles and of larger, irregular aggregates. For planar particles, a branched platelike shape with six branches, designated as shape SPp, was used (Fig. 9, upper left). With this planar shape, the horizontally projected area may be altered by changing the width of the branches. For narrow widths, the shape is much like a stellar crystal (P1d; Magono and Lee 1966) and has a small horizontally projected area. As the branch width increases, the shape approaches that of a crystal with broad branches (P1c) and at the limit of maximum branch width, is a hexagonal plate (P1a). For purposes of comparison, calculations were also done for hexagonal

plates (shape HPp) that met the mass constraints from the snow microphysics retrieval but not the constraints on horizontally projected area.

Spatial particles were represented with clusters of thick hexagonal branches and with scalene ellipsoids (Fig. 9). These spatial shapes are considered to be simplistic, somewhat abstract representations of aggregate particles. Three different configurations were examined: B6pf, with six branches all lying in the horizontal plane (Fig. 9, upper middle); B8pr-30, with eight branches, six of which intersected the horizontal plane at angles of  $30^\circ$  (Fig. 9, lower left); and B8pr-45 with eight branches, six of which intersected the horizontal plane at angles of  $45^\circ$  (Fig. 9, lower right). The orientation of the branches controls the aspect ratio of the particle and for a given aspect ratio, the horizontally projected area may be altered by changing the branch thickness. For shape B6pf, both aspect ratio and horizontally projected area get smaller as the branch thickness is reduced. Shape B8pr-30 has an aspect ratio of about 0.5, and B8pr-45 has an aspect ratio near 0.70.

The scalene ellipsoid Ep (Fig. 9, upper right) is a simple shape that also has the ability to meet the constraints on

TABLE 4. Comparison of prior and posterior PDFs for the microphysics retrieval. “Exp” is expected value, “Var” is variance, and “Cov” is covariance.

Parameter	Prior			Posterior, MH05			Posterior, HW10		
	Exp	Var	Cov	Exp	Var	Cov	Exp	Var	Cov
$\ln(\alpha)$	−6.18	2.47	0.59	−5.72	0.59	0.21	−5.68	0.59	0.20
$\beta$	2.07	0.24		2.25	0.14		2.21	0.14	
$\ln(\gamma)$	−1.56	0.39	0.12	−1.38	0.34	0.10	−1.50	0.38	0.11
$\sigma$	1.79	0.05		1.81	0.05		1.79	0.05	

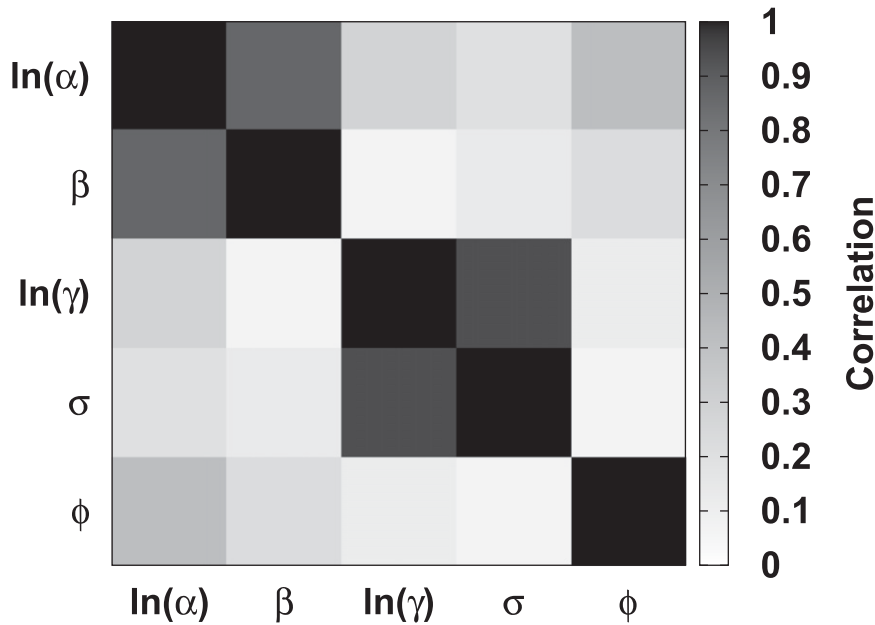


FIG. 8. Correlations between microphysical parameters.

horizontally projected area and aspect ratio, but whose shape is fundamentally different than the branched particles. Given a desired size  $D_M$ , the length of the major horizontal axis is set to this size and the length of the vertical axis is set to  $0.5D_M$ . This choice provides the same aspect ratio as the B8pr-30 shape. The length of the minor horizontal axis is adjusted to match the required horizontally projected area. In the event the required length is less than  $0.5D_M$ , the minor horizontal axis is set to  $0.5D_M$  and the required area is achieved by placing continuous porosities at random locations extending vertically through the particle.

#### b. DDA results

Scattering calculations were performed for particle sizes from  $D_M = 0.025$  mm to  $D_M = 18$  mm using the discrete dipole approximation scattering software (DDSCAT), version 7.1 (Draine and Flatau 2010). Particles were assumed to be oriented randomly with their longest dimension lying nominally in the horizontal plane (i.e., rotations in the horizontal plane were sampled uniformly), and were illuminated with a vertically incident, linearly polarized plane wave. Canting angles were applied, having values ranging over  $\pm 10^\circ$  but sampled uniformly

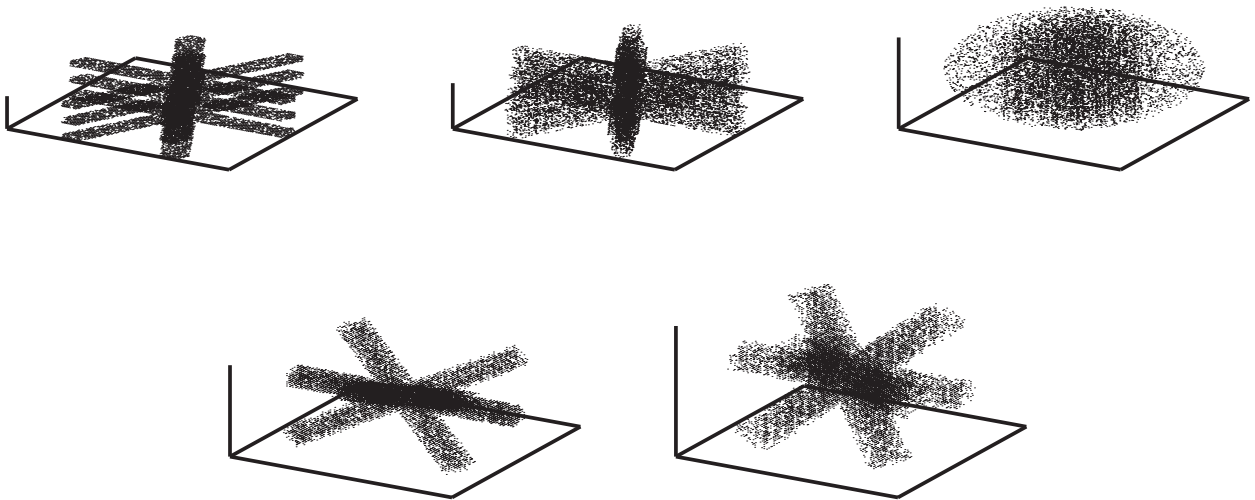


FIG. 9. Examples of shapes for dipole arrays: (top left) SPP, (top center) B6pf, (top right) Ep, (bottom left) B8pr-30, and (bottom right) B8pr-45.

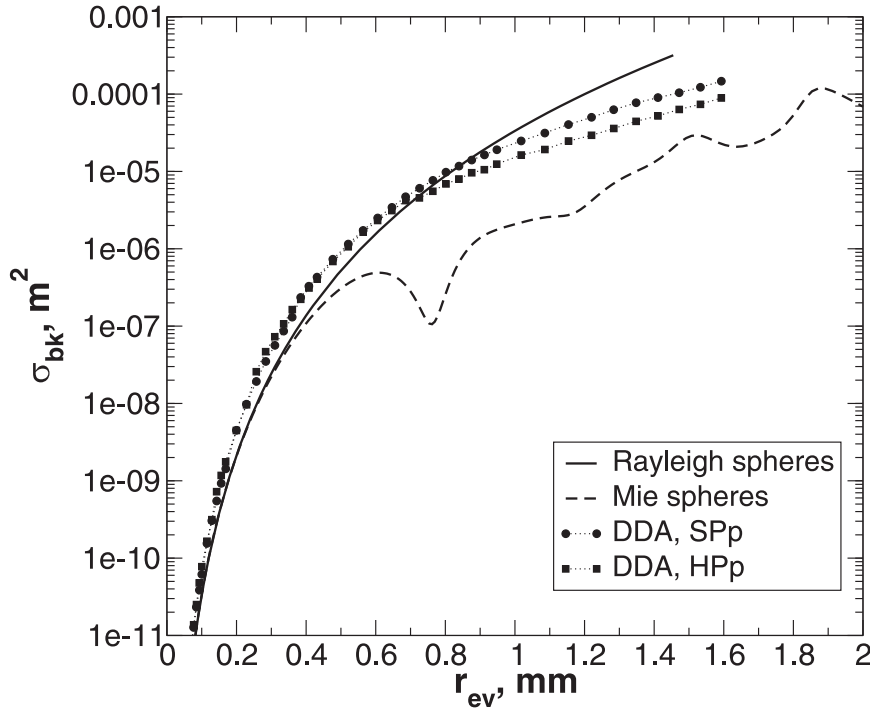


FIG. 10. Backscatter cross sections for planar particle models compared with those for Rayleigh and Mie solid ice spheres.

in the cosine of the angle following DDSCAT's standard method. This approach is an approximation based roughly on the canting angle distributions found by Matrosov et al. (2005b) for pristine dendritic particles. DDSCAT provides the differential backscatter cross section normalized by  $\pi r_{ev}^2$ :

$$Q_{bk} = \frac{1}{\pi r_{ev}^2} \left. \frac{\partial \sigma_{sca}}{\partial \Omega} \right|_{\Theta=\pi}, \quad (11)$$

where  $\Omega$  is solid angle,  $\Theta = \pi$  indicates the derivative is evaluated in the backscattering direction, and  $r_{ev}$  is the equivalent volume radius,

$$r_{ev} = \left[ \frac{m(D_M)}{\rho_{ice}} \frac{3}{4\pi} \right]^{1/3}, \quad (12)$$

with  $\rho_{ice}$  the solid ice density of  $0.917 \text{ g cm}^{-3}$ . For simulating radar reflectivities, the backscatter cross section is calculated from  $Q_{bk}$  as

$$\sigma_{bk} = 4\pi Q_{bk} \pi r_{ev}^2. \quad (13)$$

Figure 10 shows the resulting  $\sigma_{bk}$  for the planar SPp shape. For comparison,  $\sigma_{bk}$  for Rayleigh spheres, Mie spheres, and the HPp shape are shown also. Since the DDA dipoles are taken to be solid ice, as are the Rayleigh and Mie spheres, particles with the same  $r_{ev}$  contain the

same mass. For  $r_{ev}$  below about 0.7 mm,  $\sigma_{bk}$  for the SPp and HPp shapes are similar. At these small sizes, the constraint on horizontally projected area gives large area ratios, causing the SPp particles to be similar in shape to the HPp particles.

In the Rayleigh size range,  $\sigma_{bk}$  for these platelike particles exceed those for spheres, consistent with predictions by models for Rayleigh backscatter by oblate spheroids (Atlas et al. 1953). At the point where the HPp cross sections fall below those for Rayleigh spheres, the size parameter based on  $r_{ev}$ ,

$$x_{ev} = 2\pi r_{ev} / \Lambda, \quad (14)$$

where  $\Lambda$  is the radar wavelength, has a value of about 1.4. At  $r_{ev}$  larger than about 0.7 mm,  $\sigma_{bk}$  for the HPp shape fall below those for the SPp shape since HPp particles have the same mass as the SPp particles but larger horizontally projected areas. Consequently, HPp particles are thinner than the SPp, while the SPp are thicker and have much of their mass concentrated near their centers. Additionally, for  $r_{ev}$  larger than about 0.73 mm, the HPp particles have an insufficient number of dipoles to ensure that the entire plate area is occupied by dipoles. As a result, there are porosities extending through the plate. These through-porosities occupy 20%–30% of the plate area. These factors appear to be



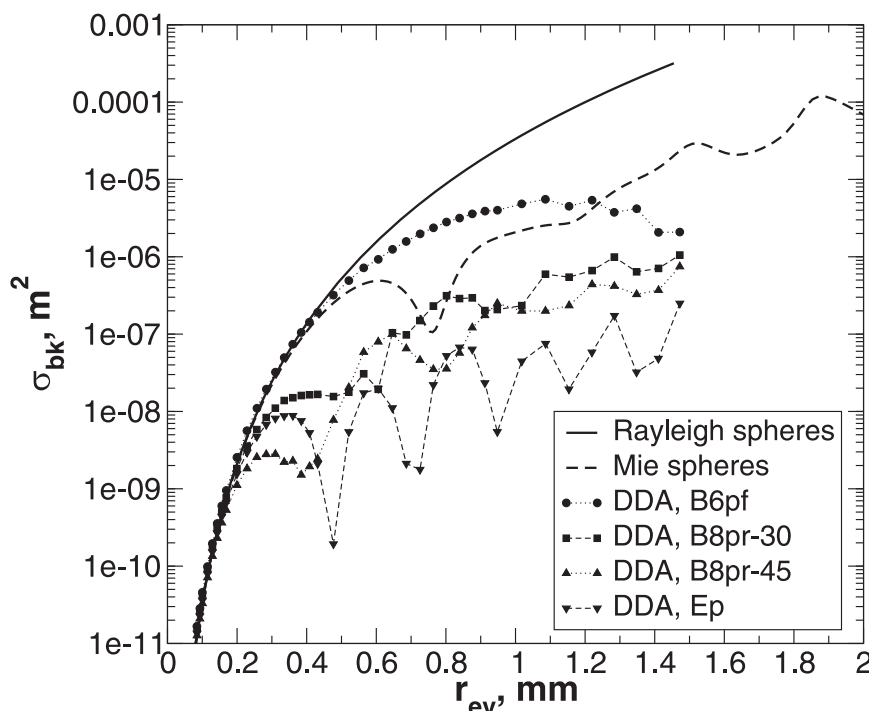


FIG. 11. As in Fig. 10, but for spatial particle models.

sufficient to cause the HPP cross sections to fall below those of the SPP particles. Neither shape shows evidence of the resonance at  $r_{ev} = 0.8$  mm that is apparent in the results for the Mie spheres.

Figure 11 shows  $\sigma_{bk}$  for the spatial particles. As before, values for Rayleigh and Mie spheres are shown for comparison. The  $\sigma_{bk}$  for the more compact shape, B6pf, are similar to those for spheres for sizes up to  $r_{ev} = 0.35$  mm. For the more spatially extended particles B8pr-30, B8pr-45, and Ep,  $\sigma_{bk}$  falls below those for Rayleigh spheres at  $r_{ev} = 0.15$  to  $0.2$  mm, corresponding to size parameters of  $0.3$ – $0.4$ . For the branched particles, as the aspect ratio of the particle increases,  $\sigma_{bk}$  decreases, although for some sizes values for B8pr-30 and B8pr-45 are almost equal. The B8pr-30 and B8pr-45 shapes show Mie-like resonances, albeit with much smaller amplitude than the Mie sphere resonance at  $r_{ev} = 0.8$  mm, while the B6pf shape shows none. The Ep shape shows markedly smaller  $\sigma_{bk}$  than the branched particles over most of the size range, and exhibits strong resonance features.

Over most of the shown size range,  $\sigma_{bk}$  for the two extremes of the branched particles (B6pf versus B8pr-45) differ by at least an order of magnitude, indicating that additional information is needed to adequately constrain the scattering properties for these spatial particles. Korolev and Isaac (2003) suggest that, for particles smaller than  $D_M = 1.0$  mm, aspect ratios should

be no larger than  $0.6$ – $0.8$ . Magono and Nakamura (1965), using photographs of snow particles taken in elevation view, found that for particles with  $D_{obs} < 10$   $\mu\text{m}$ , aspect ratios were near  $1.0$ , and that for larger particles, the horizontal dimension was substantially larger than the vertical dimension. Matrosov et al. (2005a) found that scattering models based on particles with aspect ratios of  $1.0$  gave better agreement with aircraft-observed dual-frequency radar ratios than did models based on particles with aspect ratios of  $1.0$ . These results suggest that the B8pr-30 or B8pr-45 shapes should be more representative of the backscattering properties of true snow particles, especially in larger sizes, than is the B6pf shape.

### c. Assessments

The modeled scattering properties were assessed using observed PSDs and collocated W-band radar reflectivities. PSDs were obtained from the SVI, which operated nearly continuously at CARE during the 2006/07 C3VP observing season. Observations at 1-min resolution were averaged using distinct 5-min samples as was done for the snow microphysics retrievals. These distributions, based on the Feret diameter, were converted to distributions on  $D_M$  using  $\phi = 0.78$ , the value obtained from the snow microphysics retrieval.

The observed radar reflectivities were provided by the airborne cloud radar (ACR) (Sadowy 1999), a 95-GHz

profiling radar deployed on the ground at CARE during C3VP. The ACR pointed vertically, and the range bin nearest the surface was centered at 197 m AGL. Comparisons of the reflectivities in this bin versus reflectivities in the adjacent bin above suggest this lowest bin was not substantially affected by ground clutter for reflectivities above about  $-15$  dBZ<sub>e</sub>, so observations from this lowest bin were used and assessments were limited to cases with reflectivity greater than  $-15$  dBZ<sub>e</sub>. Reflectivities in linear units at about 2.8-s resolution were averaged in time using 5-min samples, consistent with the treatment of the SVI observations. Although a formal calibration of the ACR was not performed immediately prior to C3VP, a previous intercomparison between the ACR and the University of Massachusetts Cloud Profiling Radar System showed average differences of 0.3 dBZ<sub>e</sub> (Sekelsky et al. 1999). Here, calibration errors are neglected, and it is noted that any biases in the ACR calibration could affect the results presented below.

### 1) REFLECTIVITY COMPARISONS

Data were screened for air temperatures colder than 273 K as observed on the 10-m meteorology tower at CARE. After matching observations, valid cases were obtained for twelve distinct snow events occurring over 13 days from 2 December 2006 to 26 February 2007. Attenuation in the observed ACR reflectivities is expected to be negligible because of the short range of 197 m to the selected range bin and because the radome was regularly cleared of accumulated snow by operators attending the radar during snow events (R. T. Austin et al. 2007, unpublished manuscript). For these comparisons, then, reflectivities were simulated from the modeled scattering properties assuming negligible attenuation. The unattenuated equivalent reflectivity factor for non-Rayleigh scatterers is given by

$$Z_e = \frac{\Lambda^4}{||K_w||^2 \pi^5} \int_{D_{M,\min}}^{D_{M,\max}} N(D_M) \sigma_{bk}(D_M) dD_M, \quad (15)$$

where  $K_w = (n_{liq}^2 - 1)/(n_{liq}^2 + 2)$ , and  $n_{liq}$  is the complex refractive index of liquid water. DDA backscatter efficiencies (13) were interpolated to the SVI sizes, then converted to backscatter cross sections that were used with the SVI PSDs in a discrete form of (15) to obtain simulated reflectivities.

Of the five shapes considered, the B8pr-30 shape provided the best agreement with the observed reflectivities, with a bias of  $-0.03$  dB and root-mean-square (RMS) difference of 5.4 dB over all of the PSDs that were well sampled by the disdrometer (Fig. 12). The more compact shapes B6pf and SPp substantially overestimated reflectivities over most of the observed reflectivity range and

produced considerably greater scatter versus the ACR observations. The less compact B8pr-45 and Ep underestimated reflectivities, with no improvement of RMS differences versus that for the B8pr-30 shape. Obviously, the use of the SPp shape over the full size range observed by the SVI represents an unrealistic and severe extrapolation. The largest observed  $D_M$  for this type of pristine shape (e.g., branched, stellar, or dendritic crystals) are typically a few millimeters (Heymsfield and Kajikawa 1987; Mitchell 1996), while the particle models extend to  $D_M = 18$  mm. Nonetheless, the result serves to illustrate the magnitude of errors that may be caused by the ill-considered use of such models.

The difference in bias between the B8pr-30 and the B8pr-45 shapes corresponds with differences in the vertical aspect ratios: the vertical aspect ratio for the B8pr-30 particle is about 0.5 while that for the B8pr-45 is near 0.7, giving a particle that is more extended along the direction of radar beam propagation than is the B8pr-30 shape. Additionally, for a given particle size, the branches of the B8pr-45 particle are likely somewhat wider than those of the B8pr-30 particle. This increase in width is necessary for the different shapes to have equal  $A_p$ . Wider branches would cause the B8pr-45 particle to have somewhat larger volume than the B8pr-30 particle. Since for a given size, the particles have the same mass, the dipoles in the B8pr-45 shape will not be as closely packed as in the B8pr-30 shape. In contrast, the Ep particle has the same vertical aspect ratio as the B8pr-30, but for most  $D_M$  the volume of the Ep particle substantially exceeds that of the B8pr-30, leading to a much less dense arrangement of dipoles. The resulting reflectivity bias for the Ep particle is similar to that of the B8pr-45, but the backscatter cross sections are quite different for the two shapes (Fig. 11).

Clearly, combinations of the shapes used in this study could be found that give biases similar to that of the best-fit shape. For example, one can imagine a combination of the highly reflective SPp shape at small sizes with the less reflective B8pr-45 shape at large sizes. Since these shapes are constructed using the same  $m(D_M)$  and  $A_p(D_M)$  relations, any such mixed-shape cases would give the same snowfall rates and snow water contents as the single-shape cases. In this scenario, the reflectivity bias of any mixed-shape case will simply fall between the reflectivity biases of each of the component single shapes.

The comparisons shown in Fig. 12 also highlight the possible effects of the limited sample volume of the SVI compared to the radar. The blue points are cases for which the SVI detected fewer than 100 particles over the 5-min sample with those particles distributed in five or fewer size bins, suggesting the size distributions may have been poorly sampled. An examination of the ACR

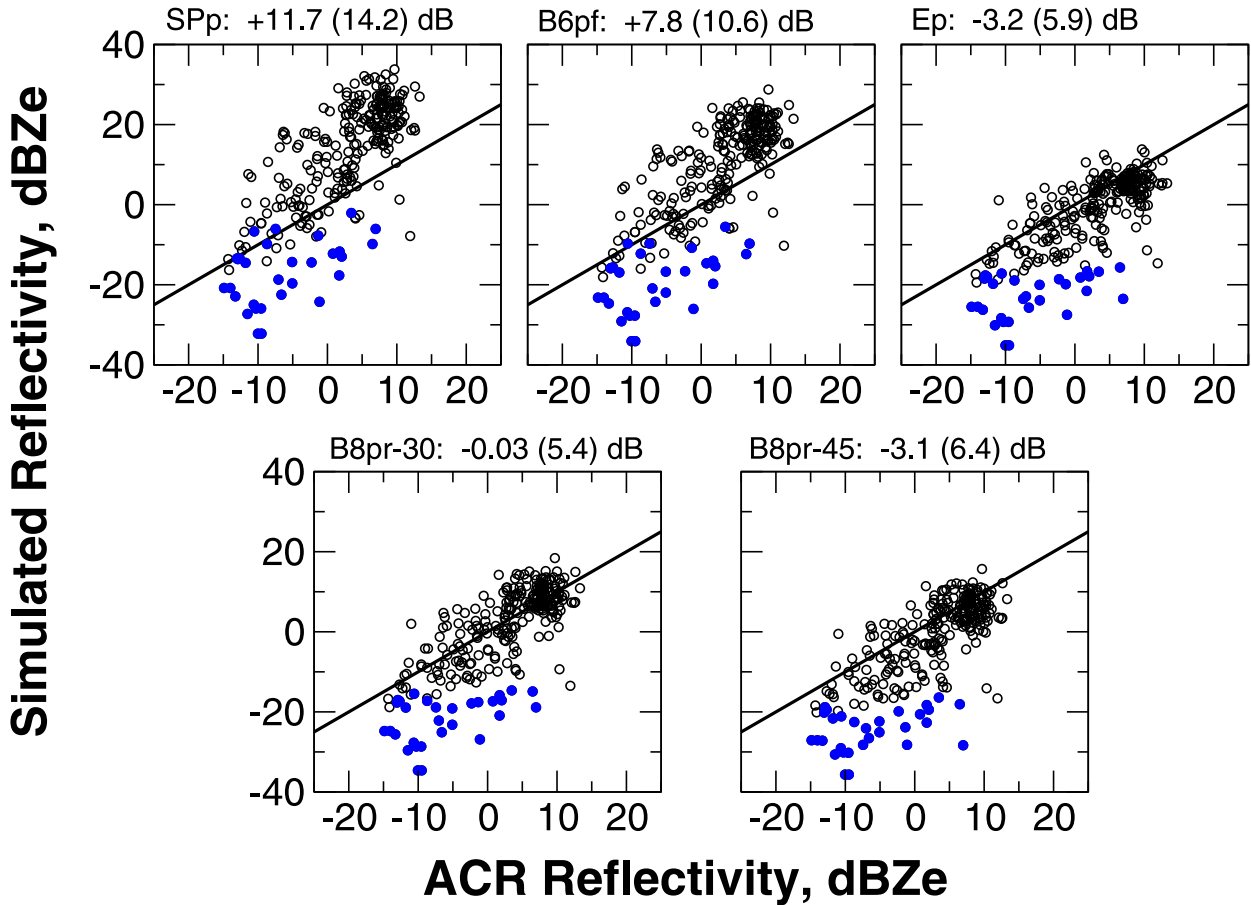


FIG. 12. Comparisons of observed W-band reflectivities from the ACR vs those simulated using DDA models for various particle shapes. The blue points indicate SVI size distributions with  $<100$  particles in the sample and with those particles distributed across five or fewer size bins. Reflectivity biases and RMS differences (in parentheses), computed over all the well-sampled (black) points, are shown above each panel.

operator's log (R. T. Austin et al. 2007, unpublished manuscript) showed that many of these cases were associated with the initiation or termination of snowfall at the surface, or with low-level stratocumulus lacking precipitation.

## 2) UNCERTAINTIES IN MODELED REFLECTIVITY

Random placement of dipoles on the lattice (appendix) causes small variations in the scattering properties. To evaluate these variations, four distinct realizations of the random dipole arrays for the B8pr-30 shape were constructed and used to calculate  $\sigma_{bk}$ . At small particle sizes, the  $\sigma_{bk}$ s were largely insensitive to the dipole locations as shown by the small fractional uncertainties (Fig. 13), consistent with the expectation that scattering properties are primarily sensitive to the mass or equivalent volume diameter in the Rayleigh regime. At larger sizes, fractional uncertainties were about 0.05, with values for particular sizes as large as 0.15 and as small as 0.015.

To evaluate the influence of random dipole locations on modeled reflectivities, the replicate realizations of the B8pr-30 scattering properties were used along with the SVI PSDs to calculate radar reflectivity per (15). Evaluations were limited to cases for which the SVI size distribution was well sampled (more than 100 particles observed or particles distributed over more than five size bins). As expected, since these random variations are uncorrelated over the range of particle sizes, the resulting uncertainties in the modeled radar reflectivity are negligible (Fig. 14), with typical fractional uncertainties in  $Z_e$  of 0.02.

The covariance matrix  $\mathbf{S}_x$  in (9) represents uncertainties in the microphysical parameters. These uncertainties contribute to uncertainties in scattering properties and thence to uncertainties in modeled reflectivities. For retrieval schemes using millimeter-wavelength radar observations, knowledge of these reflectivity uncertainties is critical. The reflectivity error variance  $s^2(Z_e)$  can be estimated using simple uncertainty propagation as

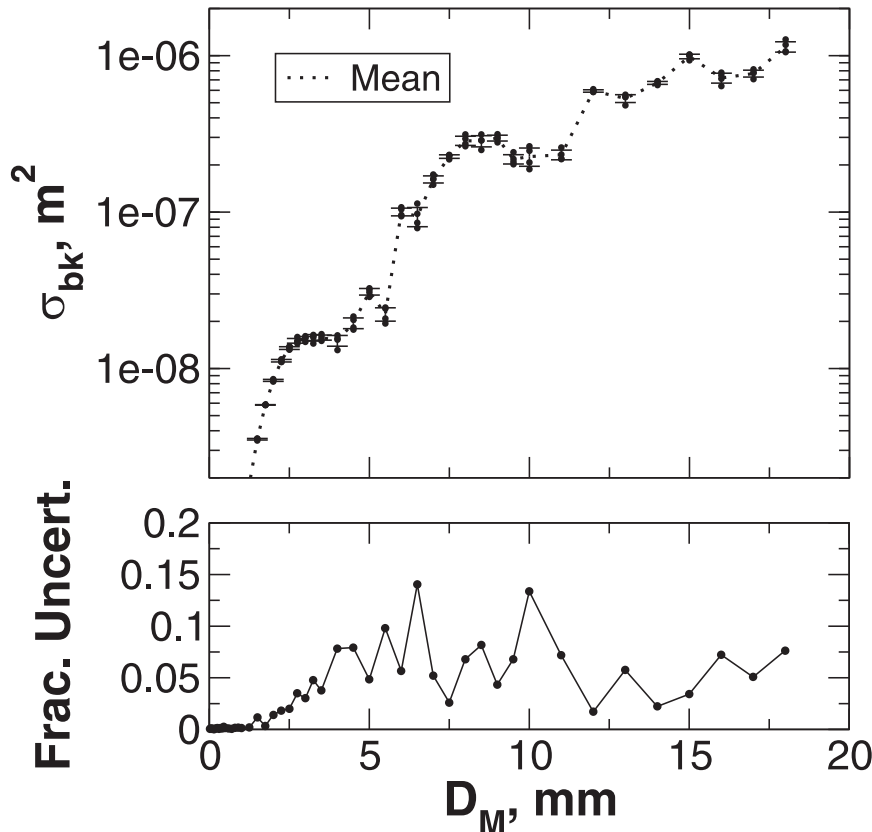


FIG. 13. The variations in  $\sigma_{bk}$  for shape B8pr-30 due to random placement of dipoles: (top) the mean and standard deviation (dotted line and error bars) along with data points from the distinct realizations, and (bottom) the fractional uncertainty for an individual realization given by the standard deviation divided by the mean value.

$$s^2(Z_e) = \mathbf{K} \hat{\mathbf{S}}_x \mathbf{K}^T, \quad (16)$$

where  $\mathbf{K}$  is the Jacobian of the modeled reflectivity with respect to the microphysical parameters

$$\mathbf{K} = \frac{\partial Z_e}{\partial \mathbf{b}} = \left\{ \frac{\partial Z_e}{\partial [\ln(\alpha)]} \quad \frac{\partial Z_e}{\partial (\beta)} \quad \frac{\partial Z_e}{\partial [\ln(\gamma)]} \quad \frac{\partial Z_e}{\partial (\sigma)} \right\}. \quad (17)$$

Evaluating Jacobian terms numerically requires that reflectivities be calculated separately with perturbed and unperturbed scattering properties. Perturbed scattering properties are obtained by perturbing each microphysical parameter then constructing new dipole arrays for each particle size, from which DDA calculations provide the perturbed scattering properties. Perturbations to the microphysical parameters must be large enough that the resulting change in  $Z_e$  is distinguishable from the uncertainty resulting from random dipole placement. If  $f_{Z_e}$  is the fractional uncertainty in  $Z_e$ , a reasonable approach (Dennis and Schnabel 1983) is to take

$$\delta b_j = \sqrt{f_{Z_e}} b_j, \quad (18)$$

where  $b_j$  is the parameter of interest. Normally  $f_{Z_e}$  is determined by the precision of the calculation of  $Z_e$ ; however, the use of random dipole locations for the

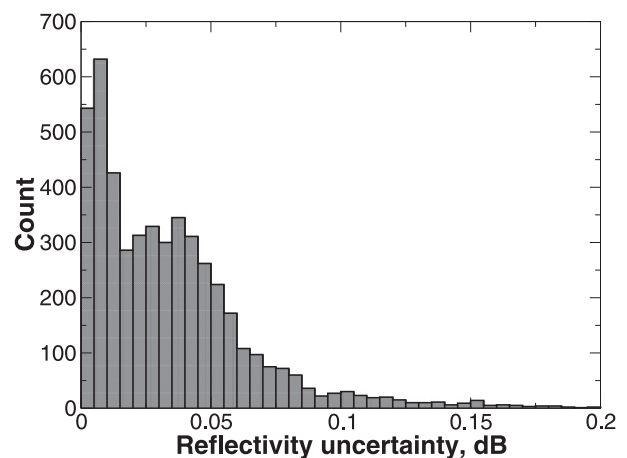


FIG. 14. Histogram of radar reflectivity uncertainties for shape B8pr-30 due to the random placement of dipoles.

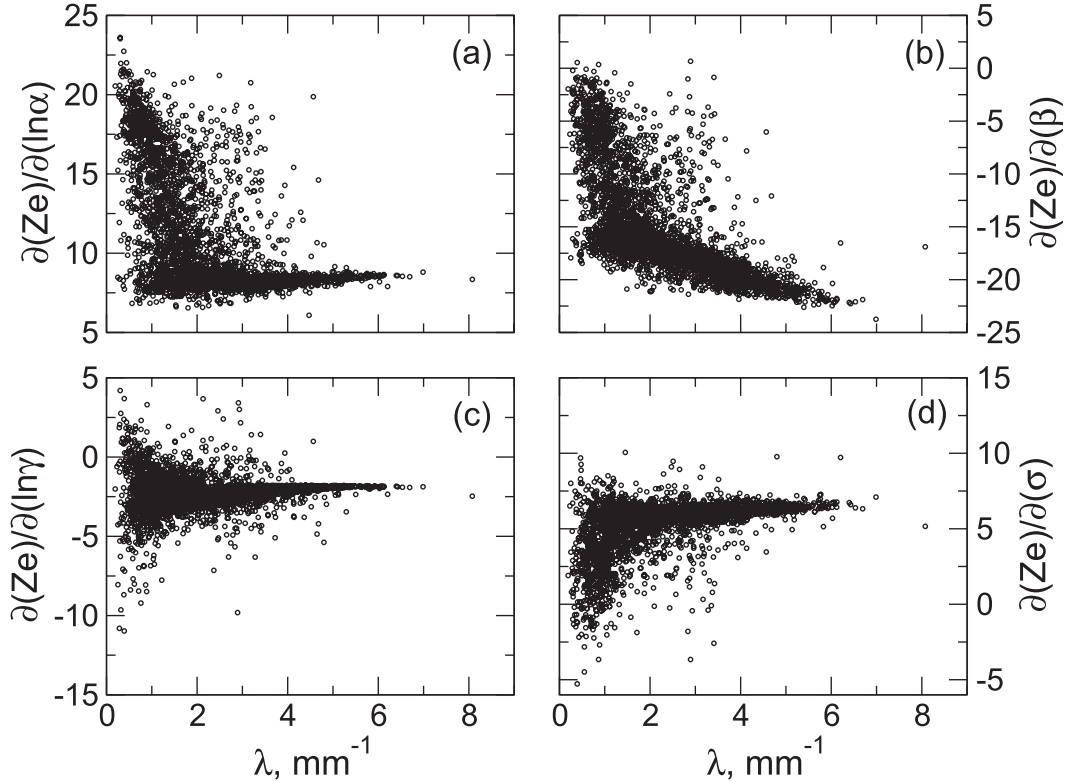


FIG. 15. Derivatives of reflectivity (dB) with respect to the microphysical parameters  $\alpha$ ,  $\beta$ ,  $\gamma$ , and  $\sigma$ . Derivatives for  $\alpha$  and  $\gamma$  are taken with respect to the natural logarithms of these parameters. Values are plotted vs the slopes  $\lambda$  of exponential size distributions fitted to the SVI PSDs.

DDA calculations of the scattering properties introduces additional uncertainties. From the results above, the fractional uncertainty for  $Z_e$  in linear units is typically less than 0.02, suggesting that  $\delta b_j \approx 0.15b_j$ , and perturbations of 15% were used.

Jacobians were evaluated using the PSDs from the SVI dataset. Reflectivity increases with increasing  $\alpha$  but decreases with increasing  $\beta$  (Figs. 15a,b). Increasing  $\alpha$  causes mass to increase over the entire size distribution, while increasing  $\beta$  causes masses to decrease for  $D_M < 1$  cm and increase for  $D_M > 1$  cm,

$$\frac{\partial m}{\partial \beta} = \frac{\partial}{\partial \beta} \alpha D_M^\beta = \alpha D_M^\beta \ln(D_M). \quad (19)$$

Negative values for  $\partial Z_e / \partial \beta$  indicate that the reflectivities are dominated by contributions from particles smaller than 1 cm. As particle size distributions broaden (indicated by decreasing  $\lambda$  in Fig. 15), the influence of large particles becomes more significant and the derivative becomes less negative. Conversely, reflectivity decreases with increasing  $\gamma$  but increases with increasing  $\sigma$  (Figs. 15c,d). Increasing  $\gamma$  causes horizontally projected areas  $A_p$  to increase over the entire

size distribution, while increasing  $\sigma$  causes  $A_p$  to decrease for  $D_M < 1$  cm and increase for  $D_M > 1$  cm, parallel to the behavior for  $\beta$ . For a given mass and shape, increasing  $A_p$  produces a less compact particle, which tends to decrease reflectivity.

Uncertainties in modeled reflectivities range from 5 to 15 dB and also depend markedly on the slope of the size distribution, with narrow distributions having much smaller uncertainties than broad distributions (Fig. 16), consistent with the behavior of the Jacobian for  $\alpha$  and  $\beta$ . It is potentially useful to know how significantly the uncertainties in individual parameters  $\alpha$ ,  $\beta$ ,  $\gamma$ , and  $\sigma$  contribute to uncertainties in the reflectivity. In the evaluation of  $s^2(Z_e)$  via (16), however, the contribution due to uncertainty in a single parameter cannot be isolated because of the presence of covariances in  $\hat{\mathbf{S}}_x$ . In an approximate sense, estimates of these contributions can be obtained from the products of the derivatives and the parameter uncertainties (Table 5). Uncertainties for the parameters were estimated as the square roots of the variances shown in (9) and derivatives were estimated as the simple means of the values shown in Fig. 15. The results suggest that uncertainties in reflectivity are dominated by contributions from  $\alpha$  and  $\beta$ .

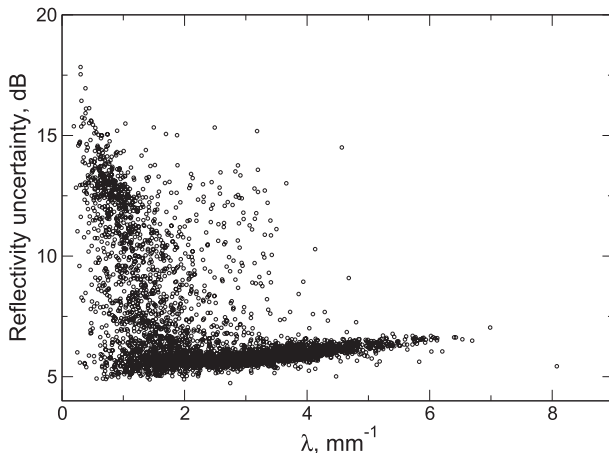


FIG. 16. Uncertainties in modeled reflectivities due to uncertainties in microphysical parameters, shown vs size distribution slope  $\lambda$ .

## 6. Conclusions

Descriptions of snow microphysical properties, consisting of expected values, uncertainties, and correlations of microphysical parameters, are essential constraints for the remote sensing of snowfall. Although estimates of parameters for mass- and area-dimension relationships for various habits are available from a number of prior studies, these studies largely lacked information needed to estimate the distributions of these parameters. Additionally, in many cases estimates of both mass and area parameters were not available from the same sample of particles, thus there was little guarantee of consistency between the mass and area representations. To address these issues, a retrieval algorithm was developed that estimates the PDFs for these microphysical properties using multisensor observations of snowfall, designed around the observations available from a highly instrumented ground site used for a snowfall remote sensing field validation campaign: Rayleigh-regime radar reflectivity, snowfall rate, particle fall speeds, and size distributions.

The algorithm was applied to observations from four snowfall events involving both synoptic front and lake-effect processes. The measurements were found to primarily determine  $\ln(\alpha)$ , and to a lesser degree  $\beta$  and  $\ln(\gamma)$ . Relatively little information was provided for  $\sigma$  and  $\phi$ . The results showed nontrivial correlations between  $\ln(\alpha)$  and  $\ln(\gamma)$ , between  $\beta$  and  $\sigma$ , and between  $\ln(\alpha)$  and  $\sigma$ . These correlations, likely the result of the dependence of fall speed on the mass-to- $A_p$  ratio, are new results that were not apparent in the a priori estimates of these parameters because of the limitations of previous analyses. These correlations form off-diagonal elements in the covariance matrix describing the multidimensional PDF for these parameters, and may have significant effects on

TABLE 5. Estimates of the contributions of uncertainties in  $\alpha$ ,  $\beta$ ,  $\gamma$ , and  $\sigma$  to uncertainties in reflectivity (dB).

Parameter	$s(\tilde{b})$	$\partial Z_e / \partial \tilde{b}$	$ s(Z_e) $
$\ln(\alpha)$	0.77	10.4	8.0
$\beta$	0.38	-16.7	6.3
$\ln(\gamma)$	0.58	-2.22	1.3
$\sigma$	0.21	5.62	1.2

Bayesian retrievals that incorporate these PDFs as a priori information. The retrieved microphysical properties are not inconsistent with observations from other sources; however, it is essential to ensure that the parameters are determined using similar definitions of particle size.

The results from these analyses provide information essential to developing physically consistent representations of snow particle microphysical and scattering properties needed by snowfall retrievals using millimeter-wavelength observations. Given the complexity of snow crystals and the highly variable shape of aggregates, the goal for such representations is to be sufficiently realistic for retrieval purposes. Particle models were constructed using the retrieved microphysical properties, and so should be consistent with observed X-band reflectivities, fall speeds, and snowfall rates. While the models did not incorporate explicit representations of pristine shapes, models with reasonable aspect ratios and inhomogeneous structure were able to reproduce observed W-band reflectivities.

Characterizing the microphysical properties in the form of PDFs allows such retrievals to better quantify forward model uncertainties, which in turn allows the uncertainties in retrieved snowfall rates to be better quantified. Using particle models constructed with the retrieved microphysical properties, we found that the uncertainties in the retrieved microphysical parameters, especially those associated with particle mass, cause substantial uncertainties in modeled reflectivities. The estimated uncertainties due to uncertainties in  $\ln(\alpha)$  (=8.0 dB) and  $\beta$  (=6.3 dB) are large compared to observational uncertainties that might be expected for W-band radars like the ACR (Sekelsky et al. 1999), and also large compared to differences among the aggregate-like Ep, B8pr-30, and B8pr-45 particles ( $\approx 3$  dB). Retrievals that account for the  $\lambda$  dependence of the reflectivity uncertainties should offer improved performance over those that do not.

The approach used to estimate these uncertainties assumes a linear error-propagation model and is likely a crude approximation for large uncertainties. Even so, in the applied context of retrievals that minimize differences between modeled and observed millimeter-wavelength radar reflectivities, these reflectivity model



uncertainties are likely significant. As demonstrated by W14, however, improvements to ground-based observing systems may better constrain microphysical properties and reduce uncertainties. Additionally, extending these analyses to a more diverse range of snowfall regimes may reveal regime-dependent variations in microphysical properties and suggest approaches to further reduce their uncertainties. Several recent field experiments, including the Light Precipitation Validation Experiment (LPVEx) and GPM Cold Season Precipitation Experiment (GCPEX), have examined snowfall in different meteorological regimes and/or used enhanced suites of instrumentation. Although the OE method developed here was targeted specifically to observations from C3VP, it is readily adaptable to observations from these and similar future experiments.

**Acknowledgments.** Parts of this research by NBW and TSL were performed at the University of Wisconsin–Madison and at Colorado State University for the Jet Propulsion Laboratory, California Institute of Technology, sponsored by the National Aeronautics and Space Administration. AJH acknowledges support from the JPL *CloudSat* Office and NASA Global Precipitation Measurement program Contract NN-X13AH73G. Computing resources for discrete dipole modeling were provided by the Community Computing Facility of the National Center for Atmospheric Research. Thanks are given to G.-J. Huang of Colorado State University, F. Fabry of McGill University, and L. Bliven of NASA Goddard Space Flight Center for making their C3VP datasets available and sharing their expertise. We appreciate the efforts of three anonymous reviewers who provided helpful feedback on the paper.

## APPENDIX

### Constrained Discrete Dipole Modeling Method

To construct a dipole array for a particle with maximum dimension  $D_M$ , first particle mass  $m$  and horizontally projected area  $A_p$  are determined using the power laws and values of  $\alpha$ ,  $\beta$ ,  $\gamma$ , and  $\sigma$  from the snow microphysics retrieval. The nondimensional area ratio  $r_A$  can then be calculated as

$$r_A = \frac{4A_p}{\pi D_M^2}. \quad (\text{A1})$$

From an assortment of nondimensional particle shapes, an instance of the shapes can be selected that matches the area ratio to within a small error, taken to be 1%.

A three-dimensional cubic lattice with lattice spacing  $d$  is defined inside the instance (Fig. A1, top). Possible

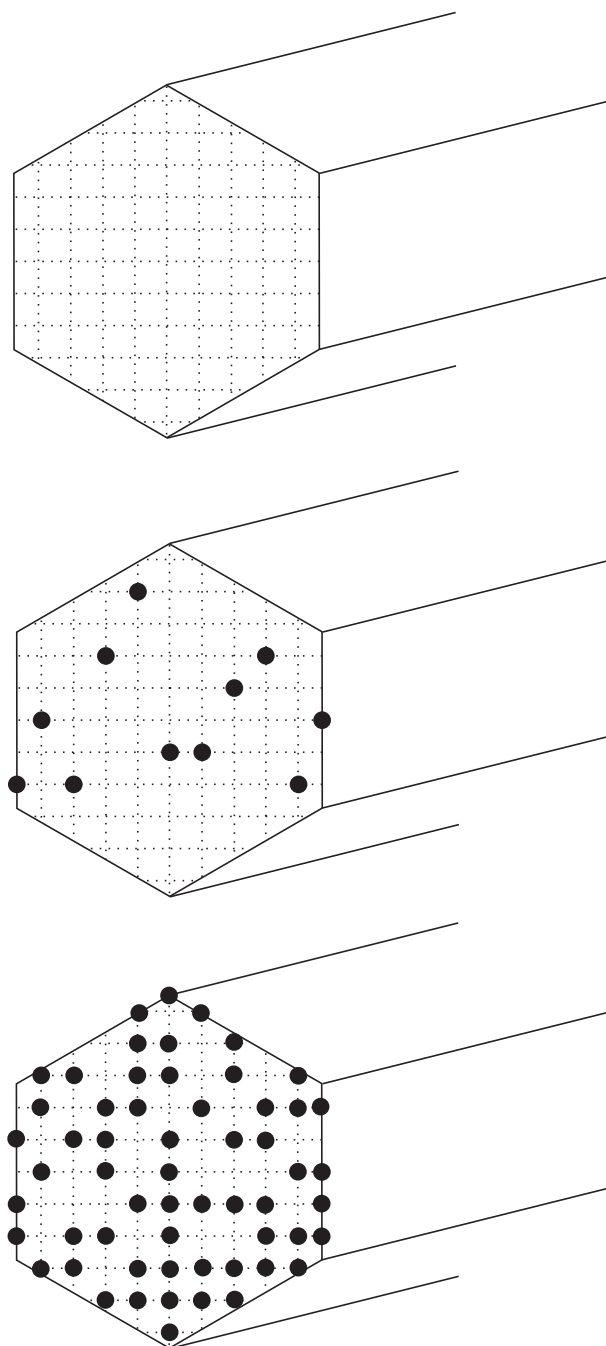


FIG. A1. Cartoon illustrating construction of a dipole array for DDA calculations. Given a desired shape that meets the specified maximum dimension and horizontally projected area, (top) first a cubic lattice is constructed within the shape. (middle) Next, dipoles are placed so that the horizontally projected area is completely occupied by dipoles. (bottom) Last, the remaining dipoles, sufficient in number to meet the specified mass, are placed randomly on the lattice.

values for  $d$  are obtained by dividing the maximum dimension  $D_M$  by integer numbers of dipoles. For accuracy when calculating  $\sigma_{bk}$ , the resulting lattice spacing should comply with

$$d < \frac{\Lambda}{4\pi|n|} \quad (\text{A2})$$

(Draine and Flatau 1994), where  $n$  is the complex refractive index of the dipole material and  $\Lambda$  is the wavelength of the incident radiation. Any spacings that do not comply are discarded. Values of  $d$  were limited to no more than  $73\text{ }\mu\text{m}$ , suitable for solid ice dipoles at 250 K and frequencies up to 183 GHz based on the ice refractive index data of Warren (1984).

Given  $d$ , the mass of a single dipole is  $d^3\rho_{\text{ice}}$  and, knowing the required particle mass  $m$ , the required number of dipoles is

$$N_{\text{dipoles}} = \frac{m}{d^3\rho_{\text{ice}}}. \quad (\text{A3})$$

If  $N_{\text{dipoles}}$  exceeds  $10^4$ , a value again based on accuracy criteria (Draine and Flatau 1994), and if the lattice has enough nodes on which to place the dipoles, the lattice spacing is acceptable. In practice, a range of  $d$  will produce acceptable lattices, so a  $d$  is chosen that makes the number of dipoles as small as possible without falling below  $10^4$ .

Dipoles are placed randomly on the lattice nodes in such a way that  $D_M$  and  $A_p$  are maintained at the required values (Fig. A1, middle and bottom). The resulting particle, rather than being solid ice, contains porosities. The porosities are normally not permitted to extend uninterrupted vertically through the particle in order to preserve  $A_p$ . This approach gives a particle model that matches the desired shape and that also matches the required  $D_M$ ,  $A_p$ , and  $m$ . The random placement of dipoles means that the modeled scattering properties will have some amount of random variation. Scattering properties at millimeter wavelengths, however, should not be strongly sensitive to the fine elements of particle structure (Matrosov 2007). Additionally, since radar reflectivity is obtained by integrating over the particle size spectrum, the effects of random variations in scattering properties on radar reflectivity should be further reduced.

## REFERENCES

- Atlas, D., M. Kerker, and W. Hitschfeld, 1953: Scattering and attenuation by non-spherical atmospheric particles. *J. Atmos. Terr. Phys.*, **3**, 108–119, doi:10.1016/0021-9169(53)90093-2.
- Boggs, P. T., R. H. Byrd, J. E. Rogers, and R. B. Schnabel, 1992: User's reference guide for ODRPACK version 2.01 software for weighted orthogonal distance regression. U.S. Department of Commerce, National Institute of Standards and Technology, Applied Computational Mathematics Division Tech. Rep. NISTIR 92-4834, 99 pp. [Available online at [http://docs.scipy.org/doc/external/odrpac\\_guide.pdf](http://docs.scipy.org/doc/external/odrpac_guide.pdf).]
- Bohren, C. F., and S. B. Singham, 1991: Backscattering by non-spherical particles: A review of methods and suggested new approaches. *J. Geophys. Res.*, **96**, 5269–5277, doi:10.1029/90JD01138.
- Brandes, E. A., G. Z. K. Ikeda, M. Schoenhuber, and R. M. Rasmussen, 2007: A statistical and physical description of hydrometeor distributions in Colorado snowstorms using a video disdrometer. *J. Appl. Meteor. Climatol.*, **46**, 634–650, doi:10.1175/JAM2489.1.
- Brown, P. R. A., and P. N. Francis, 1995: Improved measurements of the ice water content in cirrus using a total-water probe. *J. Atmos. Oceanic Technol.*, **12**, 410–414, doi:10.1175/1520-0426(1995)012<0410:IMOTIW>2.0.CO;2.
- CIRA, cited 2013: CLEX-10 daily operations page. Cooperative Institute for Research in the Atmosphere. [Available online at [http://www.wold.cira.colostate.edu/cira/GeoSci/CLEX/clex\\_main/clex10/clex10.html](http://www.wold.cira.colostate.edu/cira/GeoSci/CLEX/clex_main/clex10/clex10.html).]
- Dennis, J. E., and R. B. Schnabel, 1983: *Numerical Methods for Unconstrained Optimization and Nonlinear Equations*. Prentice-Hall, 378 pp.
- Draine, B. T., 1988: The discrete-dipole approximation and its application to interstellar graphite grains. *Astrophys. J.*, **333**, 848–872, doi:10.1086/166795.
- , and P. J. Flatau, 1994: Discrete-dipole approximation for scattering calculations. *J. Opt. Soc. Amer.*, **11A**, 1491–1499, doi:10.1364/JOSAA.11.001491.
- , and —, 2010: User guide to the discrete dipole approximation code DDSCAT 7.1. 83 pp. [Available online at <http://arxiv.org/pdf/1002.1505.pdf>.]
- Fabry, F., and I. Zawadzki, 1995: Long-term radar observations of the melting layer of precipitation and their interpretation. *J. Atmos. Sci.*, **52**, 838–851, doi:10.1175/1520-0469(1995)052<0838:LTROOT>2.0.CO;2.
- Goodison, B. E., P. Y. T. Louis, and D. Yang, 1998: WMO solid precipitation measurements intercomparison: Final report. Instruments and Observing Methods Rep. 67, WMO Tech. Doc. WMO/TD 872, 300 pp.
- Grumm, R. H., and N. A. Stuart, 2007: Ensemble predictions of the 2007 Valentine's Day winter storm. *Proc. 22nd Conf. on Weather Analysis and Forecasting/18th Conf. on Numerical Weather Prediction*, Park City, UT, Amer. Meteor. Soc., P2.49. [Available online at <http://ams.confex.com/ams/pdfpapers/123823.pdf>.]
- Heymsfield, A. J., and M. Kajikawa, 1987: An improved approach to calculating terminal velocities of plate-like crystals and graupel. *J. Atmos. Sci.*, **44**, 1088–1099, doi:10.1175/1520-0469(1987)044<1088:AIATCT>2.0.CO;2.
- , and C. D. Westbrook, 2010: Advancements in the estimation of ice particle fall speeds using laboratory and field measurements. *J. Atmos. Sci.*, **67**, 2469–2482, doi:10.1175/2010JAS3379.1.
- , C. Schmitt, and A. Bansemer, 2010: Improved representation of ice particle masses based on observations in natural clouds. *J. Atmos. Sci.*, **67**, 3303–3318, doi:10.1175/2010JAS3507.1.
- Huang, G.-J., V. N. Bringi, R. Cifelli, D. Hudak, and W. A. Petersen, 2010: A methodology to derive radar reflectivity–liquid equivalent snow rate relations using C-band radar and a 2D video disdrometer. *J. Atmos. Oceanic Technol.*, **27**, 637–651, doi:10.1175/2009JTECHA1284.1.

- Hudak, D., H. Barker, P. Rodriguez, and D. Donovan, 2006: The Canadian *CloudSat* validation project. *Proc. Fourth European Conf. on Radar in Meteorology and Hydrology*, Barcelona, Spain, ERAD, 609–612. [Available online at <http://www.crahi.upc.edu/ERAD2006/proceedingsMask/00165.pdf>.]
- , and Coauthors, 2012: GPM Cold Season Precipitation Experiment (GCPEX). *Proc. Meteorological Satellite Conf.*, Sopot, Poland, EUMETSAT, P61\_S4\_08. [Available online at [http://www.eumetsat.int/website/wcm/idc/idcplg?IdcService=GET\\_FILE&dDocName=PDF\\_CONF\\_P61\\_S4\\_08\\_HUDAK\\_V&RevisionSelectionMethod=LatestReleased&Rendition=Web](http://www.eumetsat.int/website/wcm/idc/idcplg?IdcService=GET_FILE&dDocName=PDF_CONF_P61_S4_08_HUDAK_V&RevisionSelectionMethod=LatestReleased&Rendition=Web).]
- Korolev, A., and G. Isaac, 2003: Roundness and aspect ratio of particles in ice clouds. *J. Atmos. Sci.*, **60**, 1795–1808, doi:[10.1175/1520-0469\(2003\)060<1795:RAAROP>2.0.CO;2](https://doi.org/10.1175/1520-0469(2003)060<1795:RAAROP>2.0.CO;2).
- Kruger, A., and W. F. Krajewski, 2002: Two-dimensional video disdrometer: A description. *J. Atmos. Oceanic Technol.*, **19**, 602–617, doi:[10.1175/1520-0426\(2002\)019<0602:TDVDAD>2.0.CO;2](https://doi.org/10.1175/1520-0426(2002)019<0602:TDVDAD>2.0.CO;2).
- L'Ecuyer, T. S., W. A. Petersen, and D. N. Moiseev, 2010: The Light Precipitation Validation Experiment (LPVEx): Overview and early results. *2010 Fall Meeting*, San Francisco, CA, Amer. Geophys. Union, Abstract A13K-02. [Available online at <http://abstractsearch.agu.org/meetings/2010/FM/sections/A/sessions/A13K/abstracts/A13K-02.html>.]
- Liu, C.-L., and A. J. Illingworth, 1997: Error analysis of backscatter from discrete dipole approximations for different ice particle shapes. *Atmos. Res.*, **44**, 231–241, doi:[10.1016/S0169-8095\(97\)00019-7](https://doi.org/10.1016/S0169-8095(97)00019-7).
- Locatelli, J. D., and P. V. Hobbs, 1974: Fall speeds and masses of solid precipitation particles. *J. Geophys. Res.*, **79**, 2185–2197, doi:[10.1029/JC079i015p02185](https://doi.org/10.1029/JC079i015p02185).
- Löhnert, U., S. Kneifel, A. Battaglia, M. Hagen, L. Hirsch, and S. Crewell, 2011: A multisensor approach toward a better understanding of snowfall microphysics. *Bull. Amer. Meteor. Soc.*, **92**, 613–628, doi:[10.1175/2010BAMS2909.1](https://doi.org/10.1175/2010BAMS2909.1).
- Magono, C., and T. Nakamura, 1965: Aerodynamic studies of falling snowflakes. *J. Meteor. Soc. Japan*, **43**, 139–147.
- , and C. W. Lee, 1966: Meteorological classification of natural snow crystals. *J. Fac. Sci. Hokkaido Univ. Ser. 2*, **7**, 321–335.
- Matrosov, S. Y., 2007: Modeling backscatter properties of snowfall at millimeter wavelengths. *J. Atmos. Sci.*, **64**, 1727–1736, doi:[10.1175/JAS3904.1](https://doi.org/10.1175/JAS3904.1).
- , A. J. Heymsfield, and Z. Wang, 2005a: Dual-frequency radar ratio of nonspherical atmospheric hydrometeors. *Geophys. Res. Lett.*, **32**, L13816, doi:[10.1029/2005GL023210](https://doi.org/10.1029/2005GL023210).
- , R. F. Reinking, and I. V. Djalalova, 2005b: Inferring fall attitudes of pristine dendritic crystals from polarimetric radar data. *J. Atmos. Sci.*, **62**, 241–250, doi:[10.1175/JAS-3356.1](https://doi.org/10.1175/JAS-3356.1).
- Mead, J. B., A. L. Pazmany, S. M. Sekelsky, and R. E. McIntosh, 1994: Millimeter-wave radars for remotely sensing clouds and precipitation. *IEEE Trans. Geosci. Remote*, **82**, 1891–1906.
- Mitchell, D. L., 1996: Use of mass- and area-dimension power laws for determining precipitation particle terminal velocities. *J. Atmos. Sci.*, **53**, 1710–1723, doi:[10.1175/1520-0469\(1996\)053<1710:UOMAAD>2.0.CO;2](https://doi.org/10.1175/1520-0469(1996)053<1710:UOMAAD>2.0.CO;2).
- , and A. J. Heymsfield, 2005: Refinements in the treatment of ice particle terminal velocities, highlighting aggregates. *J. Atmos. Sci.*, **62**, 1637–1644, doi:[10.1175/JAS3413.1](https://doi.org/10.1175/JAS3413.1).
- , R. Zhang, and R. L. Pitter, 1990: Mass-dimensional relationships for ice particles and the influence of riming on snowfall rates. *J. Appl. Meteor.*, **29**, 153–163, doi:[10.1175/1520-0450\(1990\)029<0153:MDRFP>2.0.CO;2](https://doi.org/10.1175/1520-0450(1990)029<0153:MDRFP>2.0.CO;2).
- Muramoto, K., K. Matsuura, and T. Shiina, 1995: Measuring the density of snow particles and snowfall rate. *Electron. Commun. Japan*, **78**, 71–79, doi:[10.1002/ecjc.4430781107](https://doi.org/10.1002/ecjc.4430781107).
- Newman, A. J., P. A. Kucera, and L. F. Bliven, 2009: Presenting the snowflake video imager (SVI). *J. Atmos. Oceanic Technol.*, **26**, 167–179, doi:[10.1175/2008JTECHA1148.1](https://doi.org/10.1175/2008JTECHA1148.1).
- Petty, G. W., and W. Huang, 2010: Microwave backscatter and extinction by soft ice spheres and complex snow aggregates. *J. Atmos. Sci.*, **67**, 769–787, doi:[10.1175/2009JAS3146.1](https://doi.org/10.1175/2009JAS3146.1).
- Rodgers, C., 2000: *Inverse Methods for Atmospheric Sounding*. World Scientific Publishing, 240 pp.
- Sadowy, G. A., 1999: A 95 GHz airborne cloud radar: Statistics of cloud reflectivity and analysis of beam-filling errors for a proposed spaceborne cloud radar. Ph.D. thesis, University of Massachusetts Amherst, 79 pp. [Available from UMI, 300 N. Zeeb Rd., Ann Arbor, MI 48103, UMI Number 9932344.]
- Schneider, T. L., and G. L. Stephens, 1995: Theoretical aspects of modeling backscattering by cirrus ice particles at millimeter wavelengths. *J. Atmos. Sci.*, **52**, 4367–4385, doi:[10.1175/1520-0469\(1995\)052<4367:TAOMBB>2.0.CO;2](https://doi.org/10.1175/1520-0469(1995)052<4367:TAOMBB>2.0.CO;2).
- Sekelsky, S. M., and Coauthors, 1999: Radar calibration validation for the SGP CART summer 1998 DC-8 cloud radar experiment. *Proc. Ninth ARM Science Team Meeting*, San Antonio, TX, U.S. Department of Energy, 1–5. [Available online at [https://www.arm.gov/publications/proceedings/conf09/extended\\_abs/sekelsky\\_sm.pdf](https://www.arm.gov/publications/proceedings/conf09/extended_abs/sekelsky_sm.pdf).]
- Shannon, C. E., and W. Weaver, 1949: *The Mathematical Theory of Communication*. University of Illinois Press, 117 pp.
- Stephens, G. L., and Coauthors, 2008: Cloudsat mission: Performance and early science after the first year of operation. *J. Geophys. Res.*, **113**, D00A18, doi:[10.1029/2008JD009982](https://doi.org/10.1029/2008JD009982).
- Vaisala Oyj, 2002: Weather sensor FD12P user's guide M210296en-A. Vaisala, 154 pp. [Available online at <http://www.vaisala.com/Vaisala Documents/User Guides and Quick Ref Guides/FD12P User Guide in English.pdf>.]
- Warren, S. G., 1984: Optical constants of ice from the ultraviolet to the microwave. *Appl. Opt.*, **23**, 1206–1225, doi:[10.1364/AO.23.001206](https://doi.org/10.1364/AO.23.001206).
- Wood, N. B., T. S. L'Ecuyer, F. L. Bliven, and G. L. Stephens, 2013: Characterization of video disdrometer uncertainties and impacts on estimates of snowfall rate and radar reflectivity. *Atmos. Meas. Tech.*, **6**, 3635–3648, doi:[10.5194/amt-6-3635-2013](https://doi.org/10.5194/amt-6-3635-2013).
- , —, A. J. Heymsfield, G. L. Stephens, D. R. Hudak, and P. Rodriguez, 2014: Estimating snow microphysical properties using collocated multisensor observations. *J. Geophys. Res. Atmos.*, **119**, 8941–8961, doi:[10.1002/2013JD021303](https://doi.org/10.1002/2013JD021303).